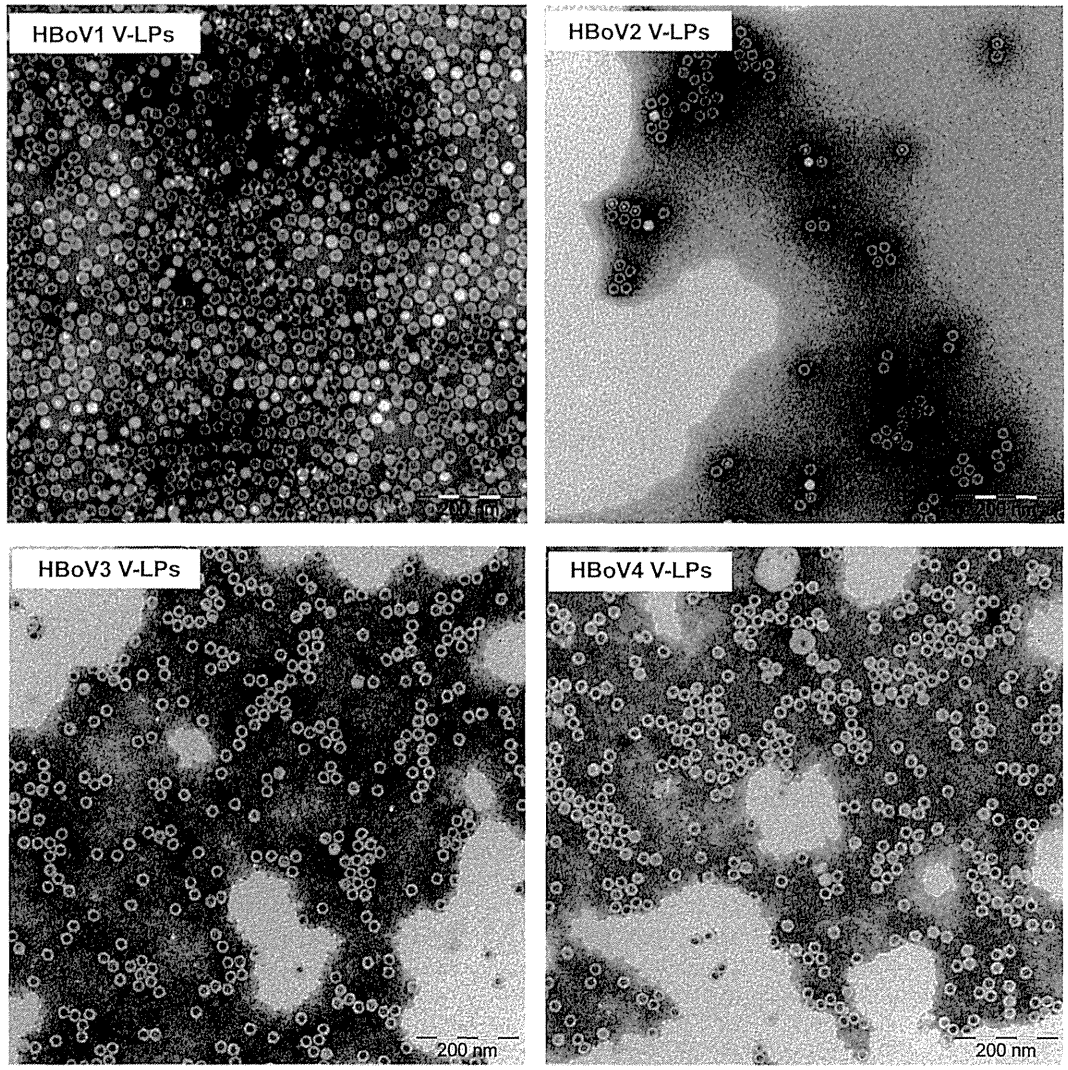

Fig. 3. Electron micrographs of HBoVLPs. The fraction containing p61 protein was stained with 2% uranyl acetate and observed by EM. Bar, 200 nm.

in all HBoVs1–4. The control VLPs derived from B19 VP2 appeared in fractions 12 and 13 with the density of 1.28 g/cm^3. The p61-containing fraction no. 8 was diluted and VLPs were sedimented by centrifugation and observed by electron microscopy. As shown in Fig. 3, empty spherical particles with an approx. 22-nm dia. were observed. The size of these particles was similar to that of the authentic HBoV particles (Brieu et al., 2007; Christensen et al., 2010; Santos et al., 2010), indicating that the recombinant VP2 self-assembled into virus-like particles (HBoV1 VLPs, HBoV2 VLPs, HBoV3 VLPs and HBoV4 VLPs). The yields of the purified HBoV VLPs obtained from 10^7 infected Tn5 cells were 1.2 mg (HBoV1 VLPs), 0.5 mg (HBoV2 VLPs), 1.0 mg (HBoV3 VLPs), and 0.8 mg (HBoV4 VLPs), respectively.

3.3. Co-expression of VP1 and VP2 proteins of HBoV1

Although VP1 of HBoV is known as a minor component of the viral particles, its role in the morphogenesis of HBoV has not yet been well determined. When HBoV1 VP1 was expressed by the recombinant baculovirus AcHBoV1-VP1 in Tn5 cells, the VP1 protein with a molecular mass of 75 kDa (p75) was detected in infected Tn5 cells. However, the expression level of the VP1 protein was quite low and not released into the culture supernatant (Fig. 4A).

In contrast, when two recombinant baculoviruses, AcHBoV1-VP1 and AcHBoV1-VP2, were co-infected to Tn5 cells, both VP1 and VP2 proteins were observed in both the cell lysate and culture supernatant (Fig. 4A). As shown in Fig. 4B, p75 and p61 appeared in the same fraction no. 8 after CsCl gradient centrifugation. Amino acids analysis showed that the N-terminal sequences of p75 was Pro-Pro-Ile-Lys-Arg, which is identical to that of the VP1 N-terminus amino acid sequence. When fraction no. 8 was observed by electron microscopy, spherical empty particles with an approx. 22-nm dia. were observed, and its morphology observed by electron microscopy was similar to that of VP2 VLPs (Fig. 4C). These results indicate that the ratio between VP1 and VP2 in a VLP is quite different if VP1 protein was incorporated into the VLP evenly. These results also suggested that the VP1 protein is a minor structural protein of HBoVs.

3.4. Antigenic cross-reactivity among HBoV VLPs

To examine the antigenicity of HBoV VLPs, rabbits were immunized with HBoV1 VLPs, HBoV2 VLPs, HBoV3 VLPs, and HBoV4 VLPs, respectively, and we determined anti-VLPs IgG titers by ELISA (Fig. 5). After three injections, all of those rabbits elicited high levels of IgG antibody against each homologous antigen at titers of 1:409,600 (HBoV1 VLPs), 1:819,200 (HBoV2 VLPs), 1:409,600

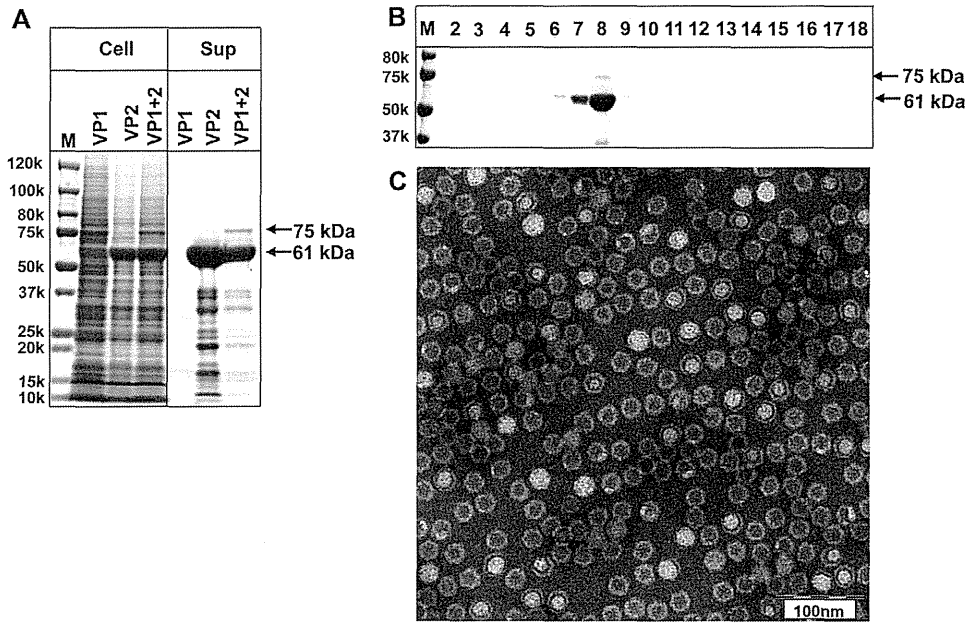

Fig. 4. Co-expression of HBoV1-VP1 and HBoV1-VP2. Insect cells (Tn5) were infected with either AcHBoV1-VP1 or AcHBoV1-VP2, or co-infected with AcHBoV1-VP1 and AcHBoV1-VP2. Expression of VP1 and VP2 proteins in cell lysates was detected at 3 days p.i. The supernatant of the infected Tn5 cells was harvested on 7 days p.i., and concentrated by ultracentrifugation. (A) The proteins were separated by SDS-PAGE and stained with Coomassie blue. (B) The VLPs recovered from the supernatant of the co-infected cells were purified by CsCl gradient centrifugation. Aliquots from each fraction were analyzed by SDS-PAGE, and stained with Coomassie blue. (C) EM of fraction no. 8. Bar, 100 nm.

(HBoV3 VLPs), and 1:819,200 (HBoV4 VLPs), respectively. None of the pre-immune sera showed any reaction against heterologous or homologous VLPs. Each serum was cross-reacted with heterologous VLPs, but the titers were lower than those with the homologous antigen. The anti-HBoV1 VLPs IgG reacted with HBoV2 VLPs, HBoV3 VLPs and HBoV4 VLPs at titers of 6400. In contrast, anti-HBoV2 VLPs IgG reacted with HBoV3 VLPs and HBoV4 VLPs at titers of 25,600, and anti-HBoV3 VLPs IgG reacted with HBoV2 VLPs and HBoV4 VLPs at titers of 204,800. Anti-HBoV4 VLPs IgG reacted with HBoV2 VLPs and HBoV3 VLPs with titers of 102,400 to 204,800, respectively. The results indicated that HBoVs are serologically cross-reactive with each other, suggesting that HBoVs possess the same antigenic epitope(s).

3.5. Seroprevalence of HBoVs in a general population in Japan

We measured the seroprevalences of anti-HBoV1, HBoV2, HBoV3 and HBoV4 IgG and IgM using 372 sera collected from healthy individuals who lived in a southern prefecture of Japan. The average positive rates of IgG were 93.0% (346/372), 70.1% (261/372), 67.7% (252/372) and 76.6% (285/372) for HBoV1, HBoV2, HBoV3 and HBoV4, respectively, whereas no significant difference was found in those of IgG among different age groups ($p < 0.05$). A high prevalence of antibodies against HBoVs was already found in the population of healthy 1- to 9-year-old children in Japan, indicating that HBoVs infection is common and the infection occurs during childhood.

The average positive rates for HBoV1, HBoV2, HBoV3 and HBoV4 in serum IgG from males and females were 93.3% and 92.9% for HBoV1, 73.9% and 68.3% for HBoV2, 68.7.6% and 65.8% for HBoV3, and 78.2% and 75.8% for HBoV4, respectively; no significant difference was seen between males and females in the IgG-positive rate for all genotypes ($p < 0.05$). In contrast to the relatively high positive rate in serum IgG, only one individual each out of the 372 (0.54%) was found to be IgM-positive for HBoV1 and HBoV3, with low OD values of 0.35 and 0.43, respectively. No serum IgM antibody against HBoV2 and HBoV4 was detectable in those serum samples.

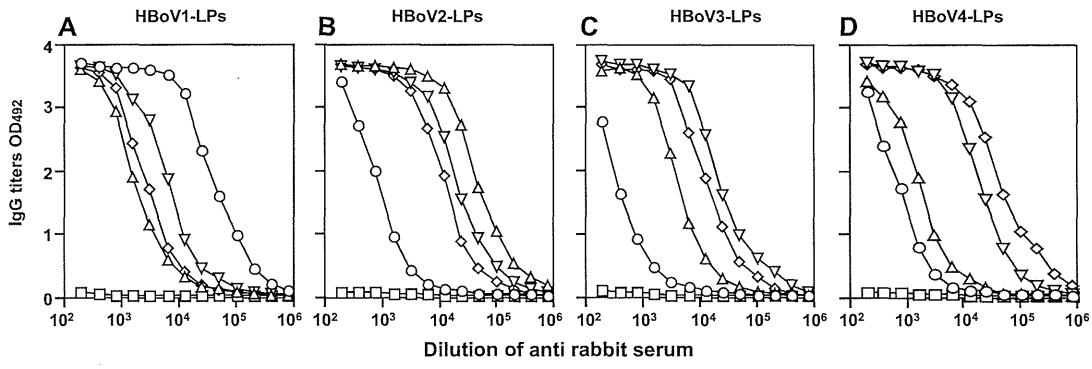

Fig. 5. Cross-reactivity among HBoVs. We prepared hyperimmune sera against HBoV1-LPs (○), HBoV2-LPs (△), HBoV3-LPs (▽) and HBoV4-LPs (◇) by inoculating rabbits with HBoVs-LPs. Cross-reactivities of HBoVs-LPs found by ELISA are shown. The ELISA was performed using HBoV1-LPs (A), HBoV2-LPs (B), HBoV3-LPs (C), and HBoV4-LPs (D) as the antigen, respectively.

4. Discussion

To date, four species of human bocavirus, HBoV1, HBoV2, HBoV3 and HBoV4, have been identified. Human bocaviruses are associated with respiratory illness and gastroenteric diseases. Because no culture system is available for HBoV growth, the serological diagnosis and vaccine development are difficult, and studies focusing on how to express the capsid protein of HBoVs are necessary. In the present study, we expressed the major capsid protein VP2 of four HBoVs in insect Tn5 cells which self-assembled into VLPs.

Recombinant baculovirus expression systems have long been used to express proteins, especially to generate VLPs of various DNA and RNA viruses. The advantages of this system are efficient expression and the self-assembly of the capsid protein into VLPs. VLPs produced by this system usually release into the cell culture supernatant and retain immunogenicity as well as physicochemical properties of their native virions (Li et al., 1997; Li et al., 2004; Murakami et al., 1999; Baumert et al., 1999; Matsuo et al., 2006). Sf9 and Tn5 cells are commonly used cell lines in baculovirus expression systems (Stewart and Possee, 1993; Wickham and Nemerow, 1993).

Previous studies have shown that the HBoV1 capsid protein VP2 expressed in Sf9 cells self-assembled into VLPs in the cell lysates, but were not released into the culture medium (Kahn et al., 2008; Soderlund-Venermo et al., 2009). Attempts were made to express the HBoV1 capsid protein VP2 in Sf9 cells, but the level of expression was significantly lower than that in Tn5, and it was difficult to obtain a larger amount of the protein (Fig. 1). In contrast, in the case of Tn5, a large amount of HBoV1 VLPs was released into the culture medium, making the purification of the VLPs much easier.

The morphologies of the VLPs derived from four genetically different HBoVs were similar. All of these VLPs had a dia. of 22 nm, similar to those of individual authentic virus particles. The density of HBoVs-LPs was approx. 1.30 g/cm^3, slightly less than that of the native virus particles, perhaps because the VLPs were empty and did not contain the virus genome. Although VLPs were obtained by the co-expression of HBoV1 VP1 and VP2, the density and morphology of the VLPs did not significantly differ from those of the VP2 VLPs. Further structural studies are needed to clarify the role of VP1 in the VLP formation.

Our immunogenic and antigenic analyses showed that HBoVs-LPs are capable of inducing IgG antibodies as high as 1:409,600 to 1:819,200 in rabbits even without any adjuvant, and we observed different degrees of cross-reactivity among the four HBoVs. The high immunogenicity of the VLPs suggests that HBoVs-LPs are promising candidates for a vaccine against HBoV infection. Phylogenetic studies have shown that the amino acid identity of VP2 among HBoVs was as high as 76.9% to 90.8%, and the antigenic cross-reactivity was confirmed in this study. Notably, based on phylogenetic analyses of the amino acid sequences deduced from the VP1/2 gene, HBoV1 shared amino acid identities of 79.4% to 79.9% with HBoV2, HBoV3, and HBoV4; however, those among HBoV2, HBoV3 and HBoV4 were 90.1% to 91.8%, suggesting that HBoV1 is slightly different from HBoV2, HBoV3, and HBoV4. In fact, the ELISA titers of anti-HBoV1 IgG against VLPs from HBoV2, HBoV3, or HBoV4 were 1:6400, weaker than other heterogeneous anti-HBoVs-LPs IgG.

Consistent with the previous findings obtained from a general population, the IgG-positive rate to HBoV1 reached 93.0% in the healthy Japanese population in the present study, indicating widespread infection in Japan. In addition, the seroprevalences of HBoV2, HBoV3, and HBoV4 were examined for the first time in a general population in Japan and were also found to be relatively high, at 70.1%, 67.7%, and 76%, respectively. Considering the cross-reactivity among HBoVs, diseases associated with HBoVs infection should be further investigated, and other immunological diagnostic methods such as the detection of HBoV-specific antigens with monoclonal antibodies are needed.

In conclusion, VLPs of four HBoVs – HBoV1, HBoV2, HBoV3 and HBoV4 – were generated by recombinant baculovirus, and their immunogenicity and antigenicity were examined. The VLPs-based ELISA results showed that HBoV infection is common in Japan. The production of HBoV VLPs will contribute to a better understanding of the epidemiology and biological characteristics of HBoVs. HBoV VLPs are also a promising resource for vaccine development.

Acknowledgements

This study was supported in part by grants for Research on Emerging and Re-emerging Infectious Diseases (no. 1-14), and Research on Hepatitis (no. 2-03) from the Ministry of Health, Labour, and Welfare of Japan. Dr. Ling Fang was supported by a Japan-China Sasagawa Medical Fellowship, the Japan-China Medical Association, and The Nippon Foundation.

References

Allander, T., Tammi, M.T., Eriksson, M., Bjerkner, A., Tiveljung-Lindell, A., Andersson, B., 2005. Cloning of a human parvovirus by molecular screening of respiratory tract samples. Proc. Nat. Acad. Sci. U.S.A. 102, 12891–12896.

Arthur, J.L., Higgins, G.D., Davidson, G.P., Givney, R.C., Ratcliff, R.M., 2009. A novel bocavirus associated with acute gastroenteritis in Australian children. PLoS Pathog. 5, e1000391.

Baumert, T.F., Vergalla, J., Satoi, J., Thomson, M., Lechmann, M., Herion, D., Greenberg, H.B., Ito, S., Liang, T.J., 1999. Hepatitis C virus-like particles synthesized in insect cells as a potential vaccine candidate. Gastroenterology 117, 1397–1407.

Brieu, N., Gay, B., Segondy, M., Foulongne, V., 2007. Electron microscopy observation of human bocavirus (HBoV) in nasopharyngeal samples from HBoV-infected children. J. Clin. Microbiol. 45, 3419–3420.

Chen, A.Y., Cheng, F., Lou, S., Luo, Y., Liu, Z., Delwart, E., Pintel, D., Qiu, J., 2010. Characterization of the gene expression profile of human bocavirus. Virology 403, 145–154.

Chow, B.D., Ou, Z., Esper, F.P., 2010. Newly recognized bocaviruses (HBoV, HBoV2) in children and adults with gastrointestinal illness in the United States. J. Clin. Virol. 47, 143–147.

Christensen, A., Nordbo, S.A., Krokstad, S., Rognlien, A.G., Dollner, H., 2010. Human bocavirus in children: mono-detection, high viral load and viraemia are associated with respiratory tract infection. J. Clin. Virol. 49, 158–162.

Dijkman, R., Koekkoek, S.M., Molenkamp, R., Schildgen, O., van der Hoek, L., 2009. Human bocavirus can be cultured in differentiated human airway epithelial cells. J. Virol. 83, 7739–7748.

Fabbiani, M., Terrosi, C., Martorelli, B., Valentini, M., Bernini, L., Cellesi, C., Cusi, M.G., 2009. Epidemiological and clinical study of viral respiratory tract infections in children from Italy. J. Med. Virol. 81, 750–756.

Gurda, B.L., Parent, K.N., Bladek, H., Sinkovits, R.S., DiMattia, M.A., Rence, C., Castro, A., McKenna, R., Olson, N., Brown, K., Baker, T.S., Agbandje-McKenna, M., 2010. Human bocavirus capsid structure: insights into the structural repertoire of the parvoviridae. J. Virol. 84, 5880–5889.

Huang, Y., Mao, P., Wang, H., 2010. Detection of, and frequent co-infection with, human bocavirus in faecal specimens from children in Wuhan, China. Clin. Microbiol. Infect. 16, 490–492.

Jartti, T., Hedman, K., Jartti, L., Ruuskanen, O., Allander, T., Soderlund-Venermo, M., 2012. Human bocavirus-the first 5 years. Rev. Med. Virol. 22, 46–64.

Kahn, J.S., Kesebir, D., Cotmore, S.F., D'Abramo Jr., A., Cosby, C., Weibel, C., Tattersall, P., 2008. Seroepidemiology of human bocavirus defined using recombinant virus-like particles. J. Infect. Dis. 198, 41–50.

Kapoor, A., Simmonds, P., Slikas, E., Li, L., Bodhidatta, L., Sethabutr, O., Triki, H., Bahri, O., Oderinde, B.S., Baba, M.M., Bukbuk, D.N., Besser, J., Bartkus, J., Delwart, E., 2010. Human bocaviruses are highly diverse, dispersed, recombination prone, and prevalent in enteric infections. J. Infect. Dis. 201, 1633–1643.

Kapoor, A., Slikas, E., Simmonds, P., Chieochansin, T., Naeem, A., Shaukat, S., Alam, M.M., Sharif, S., Angez, M., Zaidi, S., Delwart, E., 2009. A newly identified bocavirus species in human stool. J. Infect. Dis. 199, 196–200.

Li, T.C., Suzaki, Y., Ami, Y., Dhole, T.N., Miyamura, T., Takeda, N., 2004. Protection of cynomolgus monkeys against HEV infection by oral administration of recombinant hepatitis E virus-like particles. Vaccine 22, 370–377.

Li, T.C., Yamakawa, Y., Suzuki, K., Tatsumi, M., Razak, M.A., Uchida, T., Takeda, N., Miyamura, T., 1997. Expression and self-assembly of empty virus-like particles of hepatitis E virus. J. Virol. 71, 7207–7213.

Li, T.C., Yoshimatsu, K., Yasuda, S.P., Arikawa, J., Koma, T., Kataoka, M., Ami, Y., Suzaki, Y., Mai le, T.Q., Hoa, N.T., Yamashiro, T., Hasebe, F., Takeda, N., Wakita, T., 2011. Characterization of self-assembled virus-like particles of rat hepatitis E virus generated by recombinant baculoviruses. J. Gen. Virol. 92, 2830–2837.

Longtin, J., Bastien, M., Gilca, R., Leblanc, E., de Serres, G., Bergeron, M.G., Boivin, G., 2008. Human bocavirus infections in hospitalized children and adults. Emerg. Infect. Dis. 14, 217–221.

Matsuo, E., Tani, H., Lim, C., Komoda, Y., Okamoto, T., Miyamoto, H., Moriishi, K., Yagi, S., Patel, A.H., Miyamura, T., Matsuura, Y., 2006. Characterization of HCV-like particles produced in a human hepatoma cell line by a recombinant baculovirus. Biochem. Biophys. Res. Commun. 340, 200–208.

Moreno, C.M., Solis, Y.O., O'Ryan, M.G., 2009. Human bocavirus: studies in the literature and in Chile. Rev. Chil. Infectol. 26, 504–510.

Murakami, M., Gurski, K.J., Steller, M.A., 1999. Human papillomavirus vaccines for cervical cancer. J. Immunother. 22, 212–218.

Santos, N., Peret, T.C., Humphrey, C.D., Albuquerque, M.C., Silva, R.C., Benati, F.J., Lu, X., Erdman, D.D., 2010. Human bocavirus species 2 and 3 in Brazil. J. Clin. Virol. 48, 127–130.

Soderlund-Venermo, M., Lahtinen, A., Jartti, T., Hedman, L., Kemppainen, K., Lehtinen, P., Allander, T., Ruuskanen, O., Hedman, K., 2009. Clinical assessment and improved diagnosis of bocavirus-induced wheezing in children, Finland. Emerg. Infect. Dis. 15, 1423–1430.

Stewart, L.M.D., Possee, R.D., 1993. Baculovirus expression vectors. In: Davison, A.J., Elliotts, R.M. (Eds.), Molecular Virology: A Practical Approach. IRL Press, Oxford, England, pp. 227–256.

Tozer, S.J., Lambert, S.B., Whiley, D.M., Bialasiewicz, S., Lyon, M.J., Nissen, M.D., Sloots, T.P., 2009. Detection of human bocavirus in respiratory, fecal, and blood samples by real-time PCR. J. Med. Virol. 81, 488–493.

Vallet, C., Pons-Catalano, C., Mandelcwajg, A., Wang, A., Raymond, J., Lebon, P., Gendrel, D., 2009. Human bocavirus: a cause of severe asthma exacerbation in children. J. Pediatr. 155, 286–288.

Wickham, T.J., Nemerow, G.R., 1993. Optimization of growth methods and recombinant protein production in BTI-Tn-5B1-4 Insect cells using the baculovirus expression system. Biotechnol. Prog. 9, 25–30.

Biosensors and Bioelectronics 58 (2014) 33–39

Contents lists available at ScienceDirect

Biosensors and Bioelectronics

journal homepage: www.elsevier.com/locate/bios

Metal enhanced fluorescence on nanoporous gold leaf-based assay platform for virus detection

Syed Rahin Ahmed [a,b], Md. Ashraf Hossain [b], Jung Youn Park [c], Soo-Hyung Kim [b], Dongyun Lee [d], Tetsuro Suzuki [e], Jaebeom Lee [d,*], Enoch Y. Park [a,f,**]

[a] Graduate School of Science and Technology, Shizuoka University, 836 Ohya Suruga-ku, Shizuoka 422-8529, Japan
[b] Department of Nano Fusion Technology, Pusan National University, Miryang 627-706, Republic of Korea
[c] National Fisheries Research and Development Institute, Busan 619-705, Republic of Korea
[d] Department of Nano Fusion Engineering and Cogno-Mechatronics Engineering, Pusan National University, Busan 609-735, Republic of Korea
[e] Department of Infectious Diseases, Hamamatsu University School of Medicine, 1-20-1 Higashi-ku, Handa-yama, Hamamatsu 431-3192, Japan
[f] Research Institute of Green Science and Technology, Shizuoka University, 836 Ohya Suruga-ku, Shizuoka 422-8529, Japan

ARTICLE INFO

Article history:
Received 11 October 2013
Received in revised form
26 January 2014
Accepted 15 February 2014
Available online 22 February 2014

Keywords:
Nanoporous gold leaf
Surface roughness
Fluorescence enhancement
Quantum dot
Influenza A virus

ABSTRACT

In the present study, a rapid, sensitive and quantitative detection of influenza A virus targeting hemagglutinin (HA) was developed using hybrid structure of quantum dots (QDs) and nanoporous gold leaf (NPGL). NPGL film was prepared by dealloying bimetallic film where its surface morphology and roughness were fairly controlled. Anti-influenza A virus HA antibody (ab66189) was bound with NPGL and amine ($-NH_2$) terminated QDs. These biofunctionalized NPGL and QDs formed a complex with the influenza virus A/Beijing/262/95 (H1N1) and the photoluminescence (PL) intensities of QDs were linearly correlated with the concentrations of the virus up to 1 ng/mL while no PL was observed in the absence of the virus, or in bovine serum albumin (BSA, 1 μg/mL) alone. In addition, it was demonstrated that this assay detected successfully influenza virus A/Yokohama/110/2009 (H3N2) that is isolated from a clinical sample, at a concentration of ca. 50 plaque forming units (PFU)/mL. This detection limit is 2-order more sensitive than a commercially available rapid influenza diagnostic test. From these results, the proposed assay may offer a new strategy to monitor influenza virus for public health.

1. Introduction

Epidemic diseases via transmission of the virus are becoming a threatening fear for public health system; e.g., the pandemic influenza A (H1N1) 2009 virus was firstly identified in Mexico in 2009 and caused rapid outbreaks, resulting in ca. 18,000 casualties around the world (Kawai et al., 2012; Panning et al., 2009). It continues to expand globally and causes significant rates of morbidity and mortality, particularly in the elderly and children. A rapid diagnosis of influenza viruses is vital for prevention and timely control of influenza epidemics. Currently forefront tests, i.e., immunosensors and genosensors for monitoring influenza viruses at initial stage usually require professional skill, equipment, multiple processes, and low sensitivity, resulting in retardation to clinical decision (Bonanni et al., 2010; Choi et al., 2010; Deng et al., 2011; Drexler et al., 2009; Druce et al., 2005; Egashira et al., 2008; Kok et al., 2010; Kukol et al., 2008; Owen et al., 2007; Pavlovic et al., 2008; Rahman et al., 2008; van Elden et al., 2001). Numerous technologies for higher sensitivity are emerging for virus detection.

In particular, it has been attractive to utilize photoluminescence (PL) enhancement based on the near-field plasmonic effect at metallic nanostructures (Driskell et al., 2011; Gramotnev and Bozhevolnyi, 2010; Schuller et al., 2010). The interaction between metal and semiconductor nanostructure offers attractive opportunities for tuning the optical properties of such composites based on exciton–plasmon coupling. Such composite structures feature complementary optical properties; e.g., semiconductor nanostructures give rise to high emission yields and light-harvesting capabilities, whereas the metallic surface is particularly effective for local probing, confined excitation, non-linear optics and intense PL enhancement (Achermann, 2010; Lee et al., 2006, 2007). Surface roughness has long been considered as one of the

* Corresponding author. Tel.: +82 55 350 5298; fax: +82 55 350 5299.
** Corresponding author at: Research Institute of Green Science and Technology, Shizuoka University, 836 Ohya Suruga-ku, Shizuoka 422-8529, Japan. Tel./fax: +81 54 238 4887.
E-mail addresses: rahin_sust@yahoo.com (S.R. Ahmed), ashraf3521@gmail.com (Md.A. Hossain), jypark@nfrdi.go.kr (J.Y. Park), sookim@pusan.ac.kr (S.-H. Kim), dlee@pusan.ac.kr (D. Lee), tesuzuki@hama-med.ac.jp (T. Suzuki), jaebeom@pusan.ac.kr (J. Lee), acypark@ipc.shizuoka.ac.jp, acypark@icloud.com (E.Y. Park).

http://dx.doi.org/10.1016/j.bios.2014.02.039
0956-5663

critical parameters for optimizing metal enhanced fluorescence and has enabled precise control of localized surface plasmon resonance (LSPR) as well as surface plasmon polariton (SPP). In rough metallic surface, the scattering of SPP mode can produce photons that can decrease diffraction limit and resolve the sub-wavelength structure, thereby unlocking the prospect of utilizing metal–semiconductor nanocomposite films for enhancing PL emission (Ahmed et al., 2012; Leong et al., 2010; Okamoto et al., 2004).

Nanoporous gold film has unique physical properties such as excellent stability, biocompatibility, as well as high specific surface area to form self-assembled monolayers from thiols, sulfides and disulfides (Biener et al., 2008; Huang and Sun, 2005). Usually a dealloying technique is utilized to prepare nanoporous structures with controlled pore size and ligaments. By exploiting the dealloying method, PL enhancement in the vicinity of metal nanostructures can be achieved with delicate control of the morphology of the surface on the scale of a few hundreds nanometers in conjunction with interconnected-porous structures (Ciesielski et al., 2008; Detsi et al., 2011).

In the present study, the fabrication of metallic surfaces with tunable roughness and controlled structures is reported using the dealloying method. The procedure for fabrication of metal–semiconductor hybrid nanostructures was achieved by means of self-assembly techniques, and the importance of the metallic surface morphology for PL enhancement is illustrated. Furthermore, this physical study expanded to develop a highly sensitive metal–semiconductor hybrid nanostructure for the detection of influenza virus (Fig. 1).

2. Materials and methods

2.1. Materials

3-Mercaptopropionic acid (MPA; 99%), poly-diallyldimethylammonium chloride (PDDA; M.W. 400,000–500,000), polyacrylic acid (PAA; M.W.,~450,000), cadmium perchlorate hydrate, thioglycolic acid (TGA), *N*-(3-dimethylaminopropyl)-*N*′-ethylcarbodiimide (EDC) and *N*-hydroxysuccinimide (NHS) were purchased from Sigma-Aldrich (Milwaukee, USA). Aluminum telluride (Al_2Te_3) was acquired from Cerac Company (Milwaukee, USA) at the highest purity available. The chromogenic substrate, 3,3′, 5,5′-tetramethylbenzidine (TMB) was obtained from Dojindo (Osaka, Japan). Gold leaf films were purchased from Giusto Manetti Inc. (Campi Bisenzio, Italy). Anti-Influenza A virus HA H1 antibody [B219M] (ab661189, Lot: GR40088-11), anti-Swine Influenza A (H1N1) HA antibody (ab91530, Lot: 942815), and anti-H3 (H3N2) antibody [InA227] (ab82454, Lot: GR84403-3) were purchased from Abcam Inc. (Cambridge, UK). Recombinant influenza A virus HA (H1N1) (New Caledonia/20/1999; Cat: 11683-V08H) and influenza virus A/Beijing/262/95 (H1N1) (Cat: 81N73-2) were purchased from Sino Biological Inc. (Beijing, China) and HyTest Lyd. (Turku, Finland), respectively. Influenza virus A/Yokohama/110/2009 (H3N2) that was isolated from a clinical sample was kindly provided by Dr. C. Kawakami of the Yokohama City Institute of Health, Japan, and was used for confirming the versatility of the assay system. ECL™ anti-mouse IgG, horseradish peroxidase (HRP) linked whole antibody (from sheep) was purchased from GE Healthcare UK Ltd. (Buckinghamshire, UK). All other chemicals were obtained from Wako Pure Chem. Ind. Ltd. (Osaka, Japan). All experiments were carried out using high purity deionized (DI) water (> 18 MΩ).

2.2. Preparation of NPGL and semiconductor nanoparticles

The dealloying process of NPGL film has previously been described (Ciesielski et al., 2008). In this study, a gold/silver leaf was gently placed on a microscope slide. This slide was then slowly immersed into a beaker of concentrated nitric acid in order to float the leaf at the air–acid interface. The glass slide was removed when the leaf floated freely on the surface of the nitric acid solution. Subsequently, it was dealloyed for the desired time intervals of 5, 10, 30, and 60 min, and labeled as NPGL05, NPGL10, NPGL30 and NPGL60, respectively. The leaf was removed from the acid using a glass slide and transferred into a beaker containing deionized water, where the leaf was rinsed by floating for 30 min. The dealloyed leaf was withdrawn on a glass substrate that had

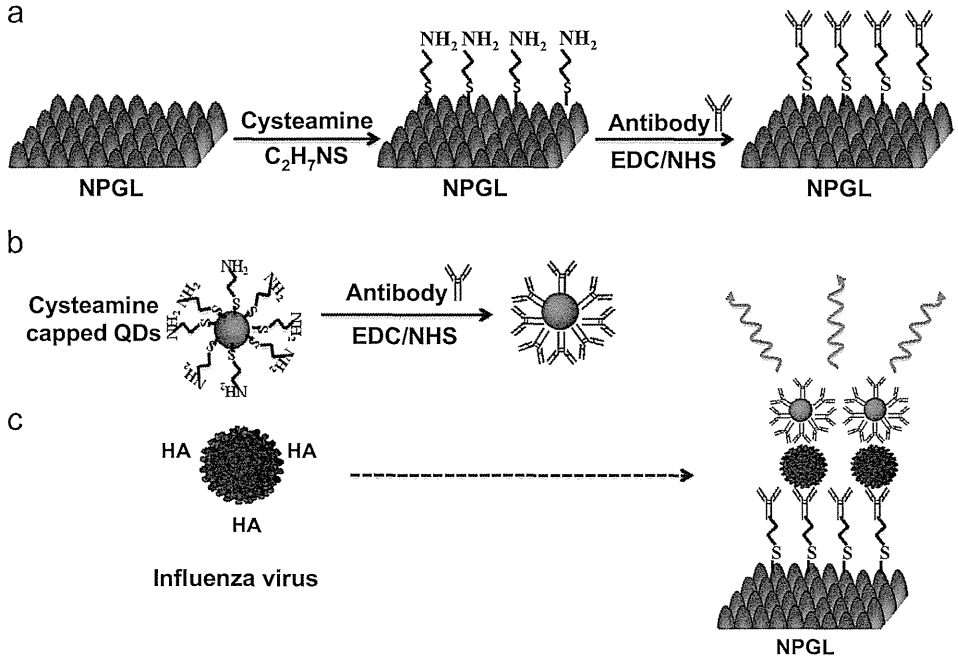

Fig. 1. Schematic of virus detection using nanoporous gold leaf (NPGL) film. The NPGL (a) and quantum dots (QDs) (b) were firstly conjugated with anti-hemagglutinin (HA) antibodies (anti-HA Ab, Y shape) by the reaction of ethylcarbodiimide (EDC)/*N*-hydroxysuccinimide (NHS). Then anti-HA Ab-conjugated with NPGL and QDs form complex (c) in presence of HA on the surface of influenza virus, finally enhancing PL intensity.

previously been modified with 3-mercaptopropyl trimethoxysilane in *n*-hexane. TGA-capped cadmium telluride (CdTe) QDs were also synthesized by a technique previously reported in detail (Gaponik et al., 2002) and stored at 4 °C prior to use.

2.3. Immobilization of CdTe QDs on the NPGL substrate

To evaluate optical properties of NPGL surface, the QDs were immobilized on the NPGL substrate by means of ultrasonic-assisted layer-by-layer (LbL) assembly (Ouyang et al., 2012; Perelshtein et al., 2008) (Supporting information S1). The polymer spacer layer of ca. 20 nm between nanocrystals and metal surface avoids unwanted quenching effects but assists PL enhancement.

2.4. Topographic observation and spectroscopic studies of NPGL films

Topographic images of the NPGL surfaces were obtained using atomic force microscopy (AFM, diInnova, Veeco, USA) and scanning electron microscopy (SEM, S4700, Hitachi High-Technol. Co., Minato-ku, Japan).

2.5. Detection platform of HA, Influenza viruses A/Beijing/262/95 (H1N1), and A/Yokohama/110/2009 (H3N2) on NPGL

Antibody specificity for HA (H1N1) was confirmed using an enzyme-linked immunosorbent assay (ELISA) (Supporting information S2) before conjugation to NPGL5 film. The anti-HA Ab (ab66189)-conjugated NPGL5 films (Supporting information S3) were rinsed 3 times with phosphate buffered saline (PBS). 100 μl anti-HA Ab-conjugated QDs (Ab-QDs) (Supporting information S1 and S4) containing different concentrations of recombinant influenza HA (H1N1) were added to the microplate wells. An Ab-QDs solution in BSA and without influenza virus HA (H1N1) was added to the same microplate as a negative control. To determine the PL enhancement effect of NPGL05 for HA detection, an identical amount of Ab-QDs solution containing 10 mg/mL HA protein was added to the wells of microplate. The microplate was then incubated for 30 min at room temperature. An infinite® F500 microplate fluorescence reader (TECAN, Männedorf, Switzerland) was employed to measure the PL intensity of each well. The samples were excited at 380 nm, and the exciting and the emission slits were 5 and 10 nm, respectively. Based on the PL values at different concentrations of HA, a dose-dependent curve was constructed. This NPGL-based assay platform was applied on detection of two different types of influenza viruses using the same protocol as described above. Influenza virus A/Beijing/262/95 (H1N1) was detected using anti-HA (H1N1) Ab-bioconjugated NPGL and QDs; influenza virus A/Yokohama/110/2009 (H3N2) was detected using anti-HA (H3N2) Ab-bioconjugated NPGL and QDs.

2.6. Detection of influenza virus by rapid influenza diagnostic test (RIDT)

To carry out direct and complementary comparison of the detection ability with commercially available influenza diagnostic kit, a commercial RIDT (ImunoAce Flu, TAUNS Lab. Inc., Numazu, Shizuoka, Japan), was purchased to detect Influenza virus A/Yokohama/110/2009 (H3N2) according to manufacturer's protocol. Different virus titers were prepared and then, three drops of virus solution were put on the sample port of the testing kit. Positive and negative influenza diagnostic results were obtained from different significant bands that appeared on the strip paper after 10 min of incubation at room temperature.

3. Results and discussion

3.1. Topographic observation of NPGL films

SEM and AFM images showed that the pore sizes of the substrates varied depending on the dealloying times (Fig. 2a–d). The size of the pores and ligaments increased with longer dealloying times due to increased removal of the less-noble constituent (silver) of the alloy. AFM was used to evaluate the root mean

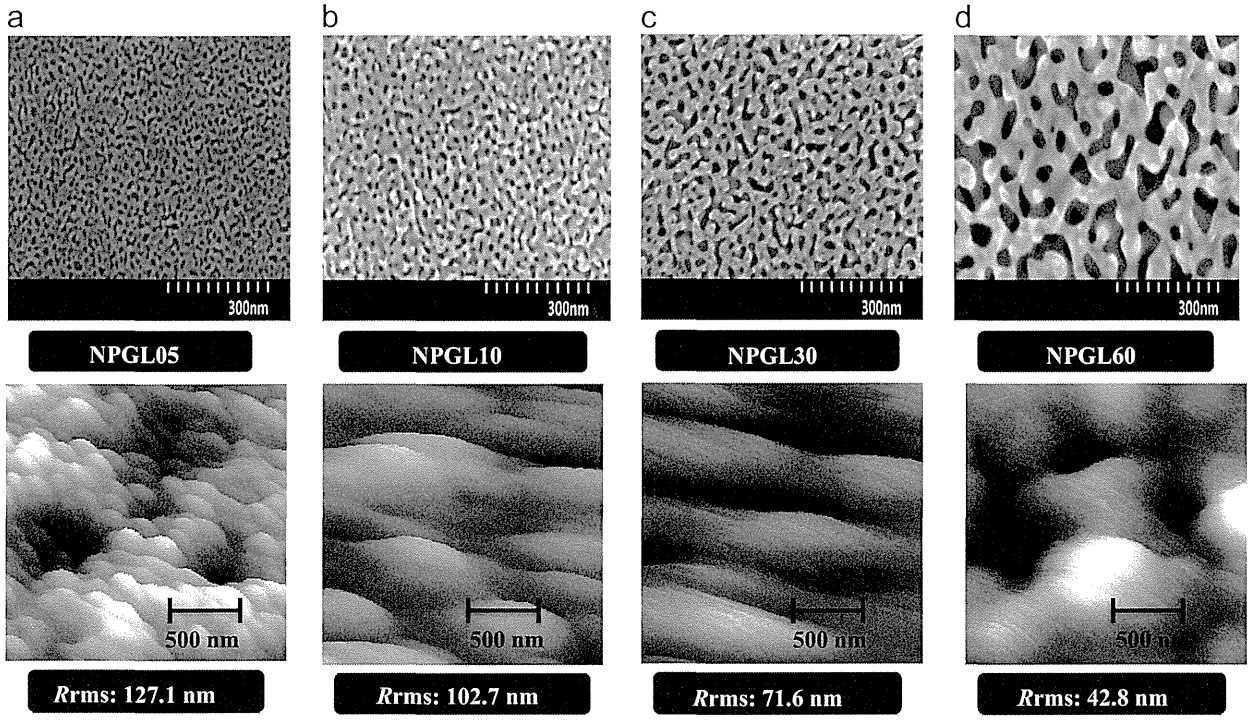

Fig. 2. SEM and AFM images and the measured R_{rms} of each NPGL sample with various dealloying times (5–60 min), where e.g., NPGL05 depicts 5 min of dealloying time. Dealloyed times are 5 min (a), 10 min (b), 30 min (c) and 60 min (d). Bars in upper and lower panels denote 300 and 500 nm respectively.

square roughness (R_{rms}) of the surface of each substrate with different dealloying times. The R_{rms} of the substrate was calculated in the scanning area ($3 \times 3\ \mu m^2$) of the AFM tip. It was found that the shorter is dealloying times the smaller is pore sizes, resulting in increasing surface irregularities and the surface roughness. Four selected NPGL samples of variant surface roughness (R_{rms} in lower panel of Fig. 2) were used for further optical evaluation.

3.2. Spectroscopic and microscopic studies of the NPGL films

The PL band of the synthesized QD solution was observed at 526 nm with a relative quantum yield of > 20% that was determined from the relative ratio versus rhodamine B dispersed in ethylene glycol, where the quantum yield of rhodamine B was 0.95 (Fig. S1A). Given that the surface roughness of each produced NPGL films differed, special care was taken in the QD immobilizing process to ensure that the equivalent amount of QDs was deposited on each substrate. Consequently, it is important to produce a monolayer of QDs on the surface of a metallic substrate. We monitored the absorbance of the QDs on the respective substrates to maintain similar intensities by adjusting the deposition time during the LbL process. Then, the PL intensity of the QD solution at the same absorption of the LbL film was measured. It was observed that the difference in the PL intensity of the various samples was less than 10%, indicating that fairly identical amount of QDs were deposited on the samples (Fig. S1B).

Indeed, PL enhancement of QDs on metal surfaces was observed. Fig. 3a shows that higher the roughness higher is the PL enhancement; e.g., the emission intensity of QDs on NPGL05 (R_{rms}=127.1 nm) and NPGL60 (R_{rms}=42.8 nm) was 9- and 2-fold higher than that on a glass substrate, respectively (Fig. 3a). When QDs were deposited on the metal surface without a spacer layer, no PL intensity was observed, rather quenching dominated. This remarkable PL enhancement may be attributed to a strong interaction with surface plasmon of metallic substrate. It has previously been reported that the excitons generated in the QDs can resonate with electron vibrations at the metal surface collectively to induce luminescence enhancement (Lee et al., 2004; Okamoto et al., 2006). Furthermore, the roughness effect on PL enhancement may be related to the multiple scattering phenomena of the SPP mode in combination with rough surfaces. Such roughness and imperfections in nanostructured random media allow SPP of high momentum to scatter and lose momentum and then couple to radioactive light (Okamoto et al., 2006). The fluorescence lifetimes (τ) of the respective samples were measured at an excitation wavelength of 380 nm using a light-emitting diode spectrophotometer (PTI Inc., USA). The spectra in Fig. 3b presents that the rougher the substrate is the shorter is the lifetime, i.e., the PL lifetime varied from 3.17 ns to 1.2 ns while the R_{rms} values varied from 42.8 to 127.1 nm (Fig. 3c). In contrast, the lifetime of CdTe QDs on glass slides was 7.42 ± 0.37 ns. In particular, the short dealloying time generated ultrafine structures that are characterized as small pores and pimples (< 10 nm) that play a major role in plasmonic scattering with consequent PL enhancement. Fig. 3d demonstrates a fluorescence microscopic image of the

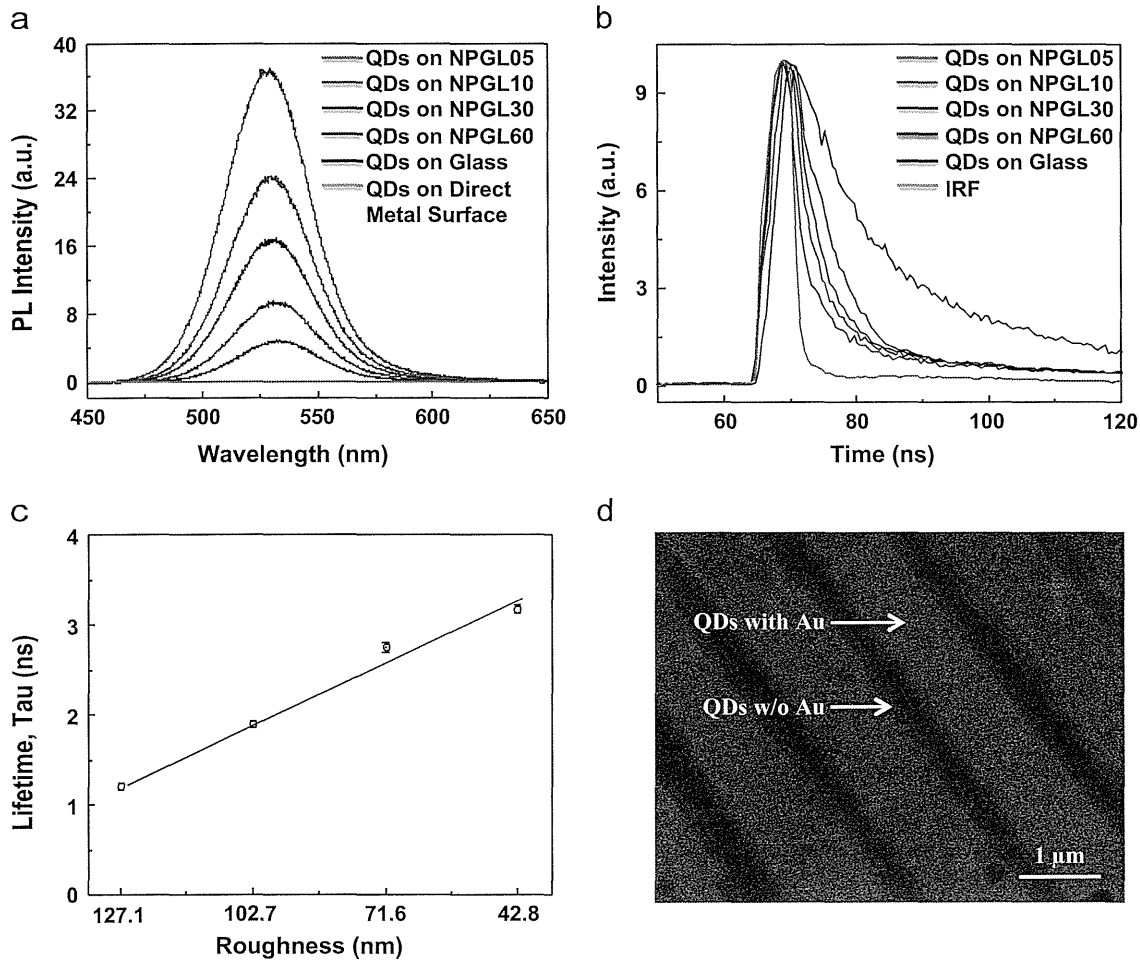

Fig. 3. (a) Photoluminescence (PL) spectra of QDs on different roughnesses of NPGL and glass substrate (for QD only); (b) time-based fluorescence kinetics profile of PL signal for QDs on different surfaces; (c) lifetimes (τ) variance depending on surface roughness; (d) fluorescence microscopic image of QDs on metallic nanostripe patterns. IRF in (b) stands for instrumental response function. The error bars in (c) indicate standard deviation (SD) in each measurement and the scale bar in (d) denotes 1 μm.

QD/polymer-deposited films on metallic nanostripe pattern to demonstrate strong PL enhancement induced by metal enhanced fluorescence. With increasing surface roughness, multiple scattering of lights occurs in nanostructured random media. The high enhancement effect observed in close proximity of metallic nanopatterns is primarily due to the absorption and/or emission bands of the QDs overlap with the scattering wavelength of the rough metallic surface. From these fundamental physical experiments NPGR05 substrate was chosen for further sensing experiments of virus detection.

3.3. Immunoassay of HA on NPGL05 and QDs

It is known that HA, a surface glycoprotein on the surface of viruses has unique immune-specificity in the initial stage of infection mechanism (Wiley and Skehel, 1987). The detailed optical observation at every respective step of bioconjugation with nanomaterials and antibodies was carefully monitored by using ELISA and FTIR spectrophotometry. Immuno-specificity of the anti-HA Ab (ab66189) for influenza virus A/Beijing/262/95 (H1N1) was investigated (Supporting information S1 and S2). A different type of Ab (ab91530) and BSA was used for comparison. A higher absorbance was observed with anti-HA Ab (ab66189) compared to the anti-HA Ab (ab91530) or BSA (Fig. S2A). From these experimental results, anti-HA Ab (ab66189) has a strong immune-specificity for influenza virus A/Beijing/262/95 (H1N1) whereas other antibody and BSA show no binding affinity with influenza A virus. The ELISA test indicated that the antibodies are successfully conjugated on the NPGLs without losing its binding affinity (Fig. S2B and C). Furthermore, FTIR bands found at 3700–3500 cm^{-1} for amide N–H stretching and 1690–1630 cm^{-1} for amide C=O stretching corresponds the chemical binding between NPGL and anti-HA Ab (ab66189) (Fig. S2D).

Then the same experiments were carried out to scrutinize any influence of binding affinity when cysteamine capped QDs were conjugated with anti-HA Ab (ab66189) using recombinant influenza H1N1 HA (New Caledonia/20/1999) (Fig. S3A), resulting that cysteamine capped QDs were successfully conjugated with the antibody (Fig. S3B and C). In fluorescence microscopic image, the aggregated and brighter spot might be virus deposited part on the film (Fig. S3D). The detection procedure consisted of three steps – (i) binding of antibody on NPGL, (ii) binding of antibody on QDs and (iii) immune-reaction between the antibody and antigen.

After confirming the binding affinity of antibody on the surface of NPGL film, the recombinant HA (H1N1) was monitored. Both NPGL film and QDs were bound with anti-HA (H1N1) Ab (ab66189). With HA, these bioconjugated components form a complex, consequently producing high PL intensity from QDs via surface plasmon resonance with the NPGL substrate. In our experiment, 3 times higher PL intensity were monitored in the nanostructure of the antibody-functionalized NPGL than that without the NPGL, where 10 μg/mL of HA was added in each experiment (Fig. 4A). In the quantitative analysis using different concentrations of HA, PL intensities were logarithmically correspondent on HA concentration in the range of 1 ng/ml–10 μg/mL (Fig. 4B and the inset). However, there was no significant PL change without any addition of HA or in the addition of BSA.

3.4. Immunoassay for virus detection

After confirmation of HA monitoring using this novel sensing system with NPGL and QDs, different concentrations of influenza virus A/Beijing/262/95 (H1N1) where the surface of this virus also has specific binding sites of anti-HA (H1N1) Ab were monitored. Similar results were observed as the previous experiment of HA only as shown in Fig. 4b. A significant PL enhancement was observed in the presence of viruses and NPGL (Fig. 5a). Furthermore, a logarithmical relationship existed between PL intensities and the virus concentration in the range of 1 ng/ml–10 μg/mL (Fig. 5b).

Using this developed monitoring system, an influenza virus A/Yokohama/110/2009 (H3N2) was monitored. The specificity of HA (H3N2) Ab 82454 for influenza virus A/Yokohama/110/2009 was confirmed (Fig. 5c), and binding of HA (H3N2) Ab 82454 with NPGL05 and QDs was also confirmed using ELISA (Fig. S4). Then, the sensitivity of influenza virus A/Yokohama/110/2009 (H3N2) detection was observed in the range of 50–10,000 plaque forming units (PFU)/mL (Fig. 5d). The detection limit was shown at ca. 50 PFU/mL.

3.5. Detection of influenza virus using rapid influenza diagnostic test (RIDT)

A commercially available RIDT kit (ImunoAce Flu, TAUNS Lab. Inc., Numazu, Shizuoka, Japan) was used for comparison with our sensing system to diagnose influenza virus infection using the influenza virus A/Yokohama/110/2009 (H3N2). Table 1 shows the results of the RIDT depending on the concentration of virus. In the case of the commercial RIDT, at least 5000 PFU/mL of virus was required for detection, which means the limit of detection (LOD) of the influenza virus detection using our sensing system of NPGL-QDs was 100 times more sensitive than that of the commercial RIDT (Fig. S5).

In this study, a new detection method on metallic surface based on exciton–plasmon interaction was presented. In particular, the

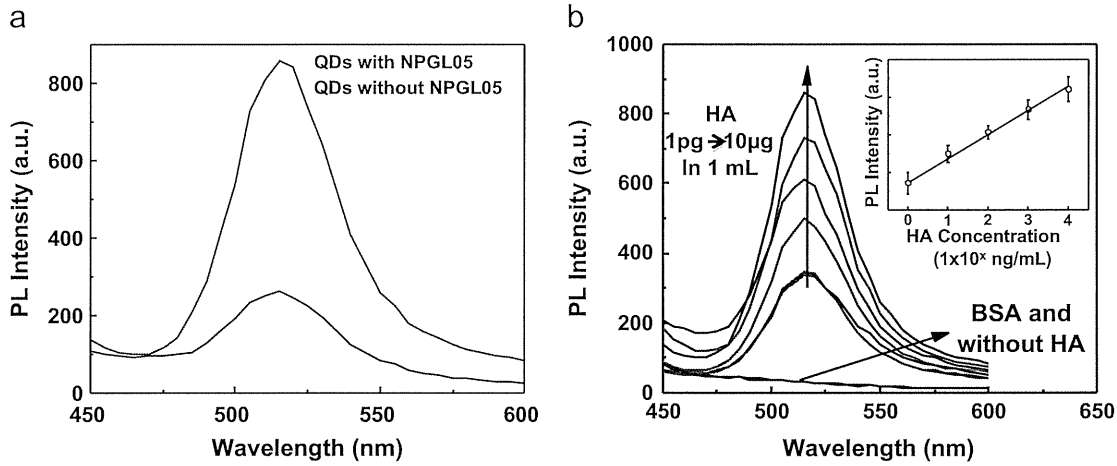

Fig. 4. (a) PL enhancement of QDs with and without the nanostructure; (b) PL enhancement corresponding on different quantities of recombinant influenza HA (H1N1) on anti-HA Ab-conjugated NPGL05. (Inset) The calibration curve of PL intensity versus HA concentration. The error bars indicate SD in each measurement.

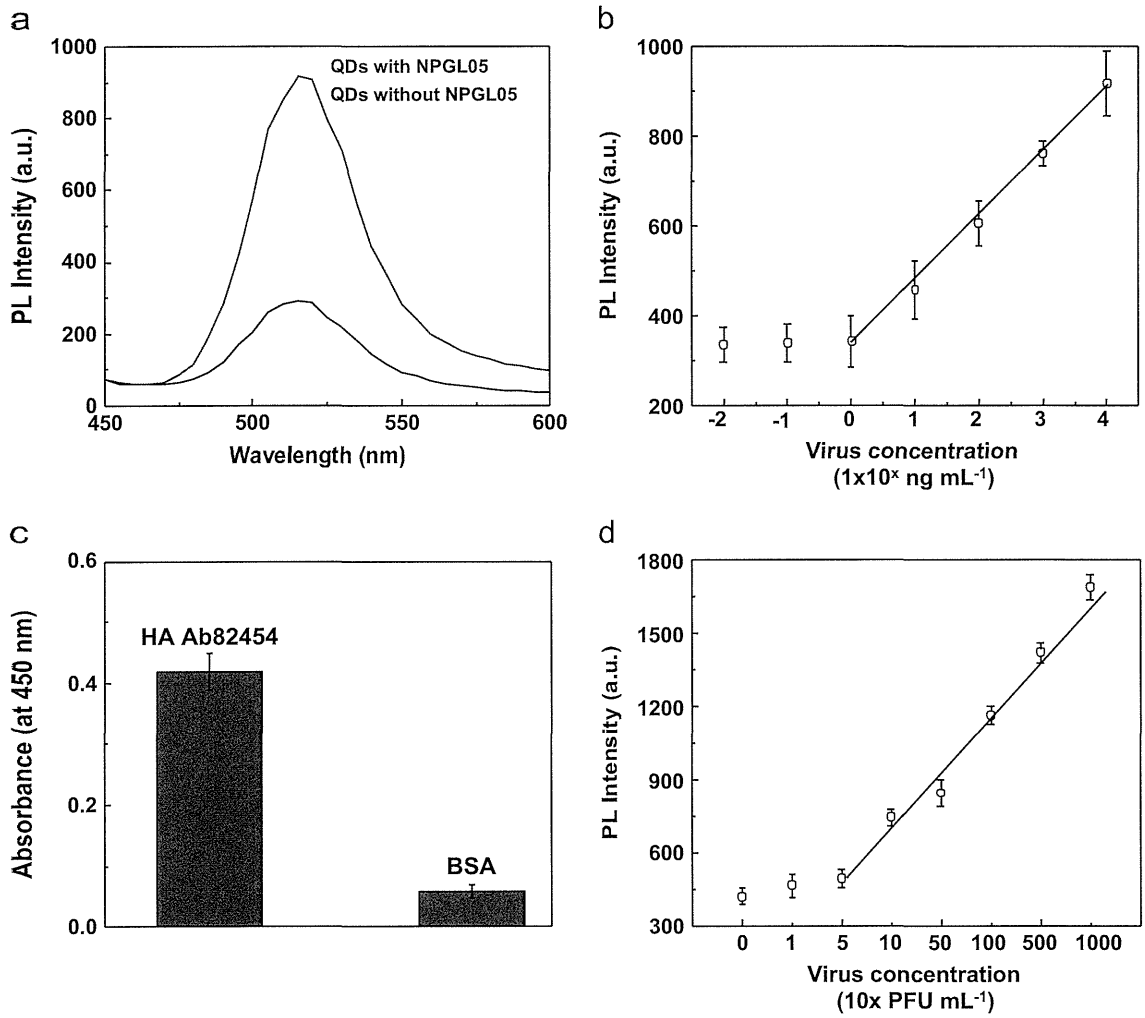

Fig. 5. (a) PL spectroscopic detection of influenza virus A/Beijing/262/95 (H1N1) using anti-HA (H1N1) Ab (ab66189)-bioconjugated QDs depending on the existence of anti-HA (H1N1) Ab (ab66189)-bioconjugated NPGL05 film; (b) PL intensity versus influenza virus A/Beijing/262/95 (H1N1) concentration; (c) ELISA results for anti-HA (H3N2) Ab 82454 binding with influenza virus A/Yokohama/110/2009 (H3N2); (d) the calibration curve of PL intensity corresponding on the concentration of the influenza virus A/Yokohama/110/2009 (H3N2). The error bars in (B–D) indicate SD (n=3).

Table 1
Comparison of influenza virus A/Yokohama/110/2009 (H3N2) detection using RIDT.

Detection method	Virus concentration (PFU/mL)								
	10,000	5000	1000	500	100	50	10	1	0
This study	+	+	+	+	+	+	−	−	−
Commercial RIDT	+	+	−	−	−	−	−	−	−

Note: + and − denote the positive and negative diagnoses, respectively.

research centered on the development of robust rough metallic surfaces that would be used for the generation of high efficient optical device for biosensor applications. Many implications for medical take care require a low detection system. An important goal here was to improve detection limit with high sensitivity. As we can see, our proposed detection method showed at least 100 times higher sensitivity than a representative commercial test kit. It might result from the presence of plasmonic rough metallic surface and adjacent control of distance between QDs to induce PL enhancement. In addition, the assay is performed with fewer amounts of reagents and easier to wash out unbound reagents. However, because of the lack of many medical samples, the huge analysis is not attainable using our technique up to now, which will be included in future work.

4. Conclusion

This paper reports a near-field optical evaluation of QDs and plasmonic surface composites with varying roughness. A dramatic enhancement of PL intensity and decay rate of the QDs was achieved on rougher metallic surfaces. The observation of these PL enhancements from nanocomposites was further applied for the development of sensitive influenza virus A (H1N1) detection (up to 1 ng/mL) and influenza A (H3N2) virus isolated from a clinical sample (up to 50 PFU/mL). The proposed method represented an alternative traditional method by requiring a higher sensitivity, much smaller sample volume, less amount reagents. Further research will be focused on the development of rough plasmonic metallic surface using self-assembly techniques as well as clinical evaluation.

Acknowledgments

We thank to Dr. Chiharu Kawakami of the Yokohama City Institute of Health, Japan, for providing influenza virus A/Yokohama/110/2009 (H3N2). This study was supported by a grant from the Korea Healthcare Technology R&D Project (A110191), the Ministry for Health, Welfare & Family Affairs, Republic of Korea;

by the National Fisheries Research & Development Institute (RP-2012-BT-030); by the Civil & Military Technology Cooperation Program through the National Research Foundation of Korea (NRF) funded by the Ministry of Science, ICT & Future Planning (No. 2013M3C1A9055407); and by the Financial Supporting Project of Long-term Overseas Dispatch of PNU's Tenure-track Faculty, 2011. This work was supported partly by Promotion of Nanobio-Technology Research to support Aging and Welfare Society from the Ministry of Education, Culture, Sports, Science and Technology, Japan. There was no additional external funding received for this study.

Appendix. Supporting information

Supplementary data associated with this article can be found in the online version at http://dx.doi.org/10.1016/j.bios.2014.02.039.

References

Achermann, M., 2010. J. Phys. Chem. Lett. 1, 2837–2843.
Ahmed, S.R., Cha, H.R., Park, J.Y., Park, E.Y., Lee, D., Lee, J., 2012. Nanoscale Res. Lett. 7, 438.
Biener, J., Nyce, G.W., Hodge, A.M., Biener, M.M., Hamza, A.V., Maier, S.A., 2008. Adv. Mater. 20, 1211–1217.
Bonanni, A., Pividori, M.I., del Valle, M., 2010. Analyst 135, 1765–1772.
Choi, Y.J., Kim, H.J., Park, J.S., Oh, M.H., Nam, H.S., Kim, Y.B., Cho, B.K., Ji, M.J., Oh, J.S., 2010. J. Clin. Microbiol. 48, 2260–2262.
Ciesielski, P.N., Scott, A.M., Faulkner, C.J., Berron, B.J., Cliffel, D.E., Jennings, G.K., 2008. ACS Nano 2, 2465–2472.
Deng, Y.M., Caldwell, N., Barr, I.G., 2011. PLoS One 6, e23400.
Detsi, E., Schootbrugge, M., Punzhin, S., Onck, P.R., Hosson, J.T.M.D., 2011. Scr. Mater. 64, 319–322.
Drexler, J.F., Helmer, A., Kirberg, H., Reber, U., Panning, M., Müller, M., Höfling, K., Matz, B., Drosten, C., Eis-Hübinger, A.M., 2009. Emerg. Infect. Dis. 15, 1662–1664.
Driskell, J.D., Jones, C.A., Tompkins, S.M., Tripp, R.A., 2011. Analyst 136, 3083–3090.
Druce, J., Tran, T., Kelly, H., Kaye, M., Chibo, D., Kostecki, R., Amiri, A., Catton, M., Birch, C., 2005. J. Med. Virol. 75, 122–129.
Egashira, N., Morita, S., Hifumi, E., Mitoma, Y., Uda, T., 2008. Anal. Chem. 80, 4020–4025.
Gaponik, N., Talapin, D.V., Rogach, A.L., Hoppe, K., Shevchenko, E.V., Kornowski, A., Eychmüller, A., Weller, H., 2002. J. Phys. Chem. B 106, 7177–7185.
Gramotnev, D.K., Bozhevolnyi, S.I., 2010. Nat. Photonics 4, 83–91.
Huang, J.F., Sun, I.W., 2005. Adv. Funct. Mater. 15, 989–994.
Kawai, Y., Kimura, Y., Lezhava, A., Kanamori, H., Usui, K., Hanami, T., Soma, T., Morlighem, J.E., Saga, S., Ishizu, Y., Aoki, S., Endo, R., Oguchi-Katayama, A., Kogo, Y., Mitani, Y., Ishidao, T., Kawakami, C., Kurata, H., Furuya, Y., Satito, Y., Okazaki, N., Chikahira, M., Hayashi, E., Tsuruoka, S., Toguchi, T., Saito, Y., Ban, T., Izumi, S., Uryu, H., Kudo, K., Sakai-Tagawa, Y., Kawaoka, Y., Hirai, A., Hayashizaki, Y., Ishikawa, T., 2012. PLoS One 7, e30236.
Kok, J., Blyth, C.C., Foo, H., Patterson, J., Taylor, J., McPhie, K., Ratnamohan, V.M., Iredell, J.R., Dwyer, D.E., 2010. J. Clin. Microbiol. 48, 290–291.
Kukol, A., Li, P., Estrela, P., Ko-Ferrigno, P., Migliorato, P., 2008. Anal. Biochem. 374, 143–153.
Lee, J., Govorov, A.X., Dulka, J., Kotov, N.A., 2004. Nano Lett. 4, 2323–2330.
Lee, J., Hernandez, P., Lee, J., Govorov, A.O., Kotov, N.A., 2007. Nat. Mater. 6, 291–295.
Lee, J., Javed, T., Skeini, T., Govorov, A.O., Bryant, G.W., Kotov, N.A., 2006. Angew. Chem. Int. Ed. 45, 4819–4823.
Leong, K., Chen, Y., Masiello, D.J., Zin, M.T., Hnilova, M., Ma, H., Tamerler, C., Sarikaya, M., Ginger, D.S., Jen, A.K.Y., 2010. Adv. Funct. Mater. 20, 2675–2682.
Okamoto, K., Vyawahare, S., Scherer, A., 2006. J. Opt. Soc. Am. B 23, 1674–1678.
Okamoto, K., Niki, I., Shvartser, A., Narukawa, Y., Mukai, T., Scherer, A., 2004. Nat. Mater. 3, 601–605.
Ouyang, J., Chang, M., Zhang, Y., Li, X., 2012. Thin Solid Films 520, 2994–2999.
Owen, T.W., Al-Kaysi, R.O., Bardeen, C.J., Cheng, Q., 2007. Sens. Actuators B – Chem. 126, 691–699.
Panning, M., Eickmann, M., Landt, O., Monazahian, M., Ölschläger, S., Baumgarte, S., Reischl, U., Wenzel, J.J., Niller, H.H., Günther, S., 2009. Eurosurveillance 14, 2003–2008.
Pavlovic, E., Lai, R.Y., Wu, T.T., Ferguson, B.S., Sun, R., Plaxco, K.W., Soh, H.T., 2008. Langmuir 24, 1102–1107.
Perelshtein, I., Applerot, G., Perkas, N., Guibert, G., Mikhailov, S., Gedanken, A., 2008. Nanotechnology 19, 245705–245710.
Rahman, M., Vandermause, M.F., Kieke, B.A., Belongia, E.A., 2008. Diagn. Microbiol. Infect. Dis. 62, 162–166.
Schuller, J.A., Barnard, E.S., Cai, W., Jun, Y.C., White, J.S., Brongersma, M.L., 2010. Nat. Mater. 9, 193–204.
van Elden, L.J., van Essen, G.A., Boucher, C.A., van Loon, A.M., Nijhuis, M., Schipper, P., Verheij, T.J., Hoepelman, I.M., 2001. Br. J. Gen. Pract. 51, 630–634.
Wiley, D.C., Skehel, J.J., 1987. Ann. Rev. Biochem. 56, 365–394.

Cytotechnology
DOI 10.1007/s10616-014-9834-9

BRIEF REPORT

Oncogenic Ras influences the expression of multiple lncRNAs

Yojiro Kotake · Madoka Naemura · Kyoko Kitagawa · Hiroyuki Niida · Toshiyuki Tsunoda · Senji Shirasawa · Masatoshi Kitagawa

Received: 7 October 2014 / Accepted: 2 December 2014

Abstract Recent ultrahigh-density tiling array and large-scale transcriptome analysis have revealed that large numbers of long non-coding RNAs (lncRNAs) are transcribed in mammals. Several lncRNAs have been implicated in transcriptional regulation, organization of nuclear structure, and post-transcriptional processing. However, the regulation of expression of lncRNAs is less well understood. Here, we show that the exogenous and endogenous expression of an oncogenic form of small GTPase Ras (called oncogenic Ras) decrease the expression of lncRNA *ANRIL* (antisense non-coding RNA in the *INK4* locus), which is involved in the regulation of cellular senescence. We also show that forced expression of oncogenic Ras increases the expression of lncRNA *PANDA* (p21 associated ncRNA DNA damage activated), which is involved in the regulation of apoptosis. Microarray analysis demonstrated that expression of multiple lncRNAs fluctuated by forced expression of oncogenic Ras. These findings indicate that oncogenic Ras regulates the expression of a large number of lncRNAs including functional lncRNAs, such as *ANRIL* and *PANDA*.

Keywords Long non-coding RNA · Oncogenic Ras · *ANRIL* · *PANDA*

Electronic supplementary material The online version of this article (doi:10.1007/s10616-014-9834-9) contains supplementary material, which is available to authorized users.

Y. Kotake (✉) · M. Naemura
Department of Biological and Environmental Chemistry, Faculty of Humanity-Oriented Science and Engineering, Kinki University, 11-6 Kayanomori, Iizuka, Fukuoka 820-8555, Japan
e-mail: ykotake@fuk.kindai.ac.jp

K. Kitagawa · H. Niida · M. Kitagawa
Department of Molecular Biology, Hamamatsu University School of Medicine, 1-20-1 Handayama, Higashi-ku, Hamamatsu, Shizuoka 431-3192, Japan

T. Tsunoda · S. Shirasawa
Department of Cell Biology, Faculty of Medicine, Fukuoka University, 7-45-1 Nanakuma, Jonan-ku, Fukuoka 814-0180, Japan

Introduction

Long non-coding RNAs (lncRNAs) range in size from 200 nucleotides to over 10 kb and are spliced and polyadenylated post-transcriptionally. Although mass scale transcriptome analysis has revealed the existence of large numbers of lncRNAs in mammals (Carninci et al. 2005), the function of most lncRNAs remain unclear. Recent studies revealed that several lncRNAs are involved in biological processes including development, cellular senescence, apoptosis, and cancer (Batista and Chang 2013; Fatica and Bozzoni 2014; Kitagawa et al. 2013, 2012). Previously, we and another group have reported the role of the lncRNA *ANRIL* (antisense non-coding RNA in the *INK4* locus)

Journal : Medium 10616 | Dispatch : 4-12-2014 | Pages : 5
Article No. : 9834 | ☐ LE | ☐ TYPESET
MS Code : CYTO-D-14-00229 | ☑ CP | ☑ DISK

in the regulation of *INK4* locus (Kotake et al. 2011; Yap et al. 2010), which encodes two cyclin-dependent kinase inhibitors, $p15^{INK4B}$ and $p16^{INK4A}$ and a positive regulator of p53, *ARF*. The *INK4* locus is frequently mutated or its expression is silenced in human cancers (Ruas and Peters 1998; Sharpless 2005). *ANRIL* (3.8 kb transcript) is expressed in the opposite direction from the $p16^{INK4A}$-*ARF*-$p15^{INK4B}$ gene cluster. *ANRIL* binds to polycomb repression complex 1/2, that stably silence gene expression and is required for the recruitment and repression of $p15^{INK4B}$ and $p16^{INK4}$ transcription, resulting in the prevention of cellular senescence. *PANDA* (p21 associated ncRNA DNA damage activated; 1.5 kb transcript) is a p21 promoter-derived lncRNA induced by DNA damage in a p53-dependent manner (Hung et al. 2011). *PANDA* directly binds to the transcription factor NF-YA and inhibits its association with promoters of pro-apoptotic genes, such as *FAS*, *NOXA*, and *PUMA*. Depletion of *PANDA* sensitizes cells to apoptosis by DNA damage, suggesting that *PANDA* functions by blocking apoptosis to maintain the survival of cells that have sustained DNA damage.

Recent studies have revealed that several lncRNAs, such as *MALAT1* and *HOTAIR*, are also associated with cancer progression (Gupta et al. 2010; Tano et al. 2010). Although the biological importance of lncRNAs has gradually been demonstrated, the regulation of lncRNAs expression is poorly understood. In this study, we analyzed the expression of lncRNAs induced by oncogenic Ras signaling.

Materials and methods

Cell culture and retroviral transduction

WI38 and TIG-3 cells are normal human diploid fetal lung fibroblasts. WI38 cells were obtained from American Type Culture Collection (Frederick, MD) and TIG-3 cells were obtained from Health Science Research Resource Bank (Osaka, Japan). Human colorectal cancer HCT116 cells were obtained from American Type Culture Collection (Frederick, MD). HKe3 cells were established from HCT116 cells with a disruption in oncogenic K-Ras (Shirasawa et al. 1993). All cells were cultured in DMEM containing 10 % fetal bovine serum. WI38 and TIG-3 cells were infected with retroviruses expressing $H\text{-}Ras^{G12V}$ (kindly provided by Dr. CJ. Der, University of North Carolina at Chapel Hill, Chapel Hill, NC, USA). The pMX-puro retrovirus vector was kindly provided by Dr. T Kitamura (The University of Tokyo, Tokyo, Japan). Retrovirus production and transduction were performed as previously described (Kotake et al. 2007).

Western blotting

For western blotting, cells were lysed with RIPA buffer (50 mM Tris–HCl pH 8.0, 150 mM NaCl, 1 % NP-40, 0.5 % DOC, 0.1 % SDS, 1 mM Na_3VO_4, 1 mM DTT, 1 mM PMSF) supplemented with protease inhibitors (10 mg/L antipain, 10 mg/L leupepcin, 10 mg/L pepstatin, 10 mg/L trypsin inhibitor, 10 mg/L E64, and 2.5 mg/L chymostatin). Western blotting was performed as previously described (Kotake et al. 2007). Antibodies to H-Ras (OP23; Calbiochem) and α-tubulin (Sigma) were purchased commercially.

Reverse transcription-polymerase chain reaction (RT-PCR)

For RT-PCR, total RNA was extracted by RNeasy Plus kit (Qiagen), and 1 μg of total RNA was used for cDNA synthesis primed with oligo dT primers (Invitrogen). The specific PCR pairs for *PANDA*, *ANRIL*, and *GAPDH* were as follows: *PANDA*, 5′-AGACCC CAGTGGCACCTGAC-3′ and 5′-GGGCAGAACTT GGCATGATG-3′; *ANRIL*, 5′-TGCTCTATCCGCCA ATCAGG-3′ and 5′-GGGCCTCAGTGGCACATA CC-3′; *GAPDH*, 5′-GCAAATTCCATGGCACCGT-3′ and 5′-TCGCCCCACTTGATTTTGG-3′.

DNA microarray

DNA microarray analysis was performed using SurePrint G3 Human GE 8x60K (Agilent Technologies) according to the manufacturer's protocol by Hokkaido System Science. Three chips per group were hybridized. Briefly, total RNA was extracted by RNeasy Mini kit (Qiagen), and 200 μg of total RNA was amplified and labeled with cyanine 3 CTP by the Low Input Quick Amp Labeling kit (Agilent Technologies). Labeled cRNA was purified by RNeasy mini spin column (Qiagen) and 600 ng of cyanine 3 labeled cRNA was hybridized to SurePrint G3 Human GE 8x60K (Agilent Technologies). The chips were analyzed by Agilent Technologies Microarray Scanner.

Journal : Medium 10616 | Dispatch : 4-12-2014 | Pages : 5
Article No. : 9834 | ☐ LE | ☐ TYPESET
MS Code : CYTO-D-14-00229 | ☑ CP | ☑ DISK

Results and discussion

The small GTPase Ras controls cell proliferation, survival, and differentiation by regulating downstream effector molecules, such as mitogen-activated protein kinases, phosphoinositide 3-kinase, and Ral guanine nucleotide-dissociation stimulator (Karnoub and Weinberg 2008; Schubbert et al. 2007). Activating Ras mutations including G12V and G13D amino acid substitution lead to oncogenic transformation and occur in a wide range of human cancers. Previously and here, we showed that *ANRIL* expression is decreased by forced expression of H-Ras^{G12V} in WI38 cells (Kotake et al. 2011) (Fig. 1a, b). Furthermore, we examined by using HCT116 and HKe3 cells whether endogenous expression of oncogenic Ras affect the expression of *ANRIL*. HCT116 cells have a heterozygous K-Ras mutation (G13D). HKe3 cells were generated by disrupting the K-Ras^{G13D} of HCT116 cells (Shirasawa et al. 1993). RT-PCR analysis demonstrated that *ANRIL* is expressed at a low level in HCT116 cells as compared to HKe3 cells (Fig. 1c). We also examined the effect of oncogenic Ras on the expression of *PANDA*. The stable cell lines expressing H-Ras^{G12V} in TIG-3 cells in which *PANDA* expression was detectable were established, and the expression of *PANDA* was determined. Western blotting results demonstrated the stable expression of H-Ras^{G12V} (Fig. 2a). *PANDA* expression was substantially increased by H-Ras^{G12V} transduction as assessed by RT-PCR analysis (Fig. 2b). These data indicate that oncogenic Ras regulates the expression of two lncRNAs, *ANRIL* and *PANDA*, which have a pivotal role in cell fate determination, such as cellular senescence and apoptosis.

Oncogenic Ras might also affect other lncRNAs. Therefore, we next examined the effect of oncogenic Ras on the expression of lncRNAs by global analysis. DNA microarray analysis showed that 3,373 of the protein coding genes (PCG) had at least a twofold change by H-Ras^{G12V} transduction (Fig. 3a; Table 1). These data support a previous study demonstrating oncogenic Ras regulates diverse pathways (Karnoub and Weinberg 2008). Additionally, of the 7,419 transcribed regions of lncRNAs, the expression level of 243 (3.3 %) increased more than twofold and the expression level of 168 (2.3 %) decreased by <50 % following H-Ras^{G12V} transduction (Fig. 3b; Table 1 and Supplemental Table 1). These data indicate that oncogenic Ras regulates the expression of multiple lncRNAs as well as PCG.

In this paper, we showed that both exogenous and endogenous expression of oncogenic Ras decreased the expression of *ANRIL*, which represses the transcription of *INK4* locus. In mouse and human fibroblasts, the transcription of *INK4* locus is activated by oncogenic Ras, causing stable cell cycle arrest to protect cells from hyperproliferative stimulation

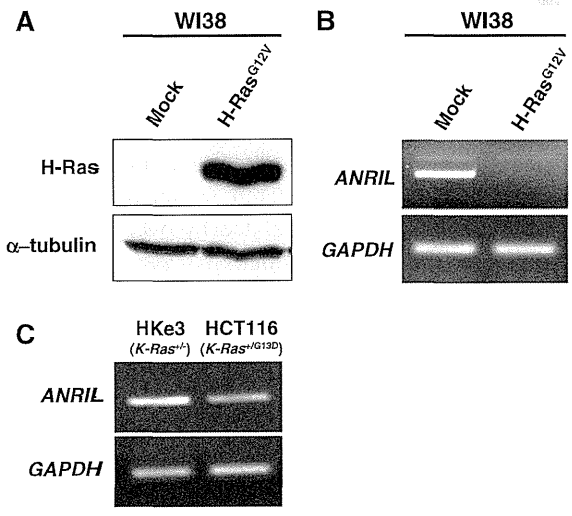

Fig. 1 Effect of oncogenic Ras on *ANRIL* expression. WI38 cells were infected with control (Mock) or H-Ras^{G12V}-expressing retroviruses and selected by puromycin. H-Ras protein levels were determined by western blotting (**a**). The levels of *ANRIL* expression were determined in WI38/Mock and WI38/H-Ras^{G12V} cells by RT-PCR (**b**). The levels of *ANRIL* expression were determined in HKe3 and HCT116 cells by RT-PCR (**c**)

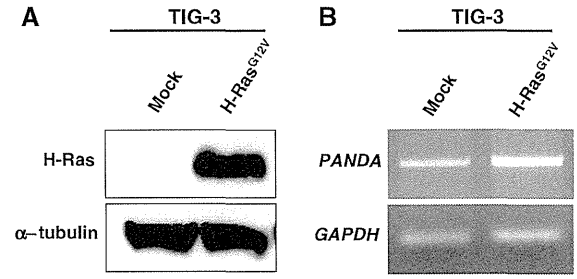

Fig. 2 Effect of oncogenic Ras on *PANDA* expression. TIG-3 cells were infected with control (Mock) or H-Ras^{G12V}-expressing retroviruses and selected by puromycin. H-Ras protein levels were determined by western blotting (**a**). The levels of *PANDA* expression were determined in TIG-3/Mock and TIG-3/H-Ras^{G12V} cells by RT-PCR (**b**)

Journal : Medium 10616 | Dispatch : 4-12-2014 | Pages : 5
Article No. : 9834 | LE | TYPESET
MS Code : CYTO-D-14-00229 | CP | DISK

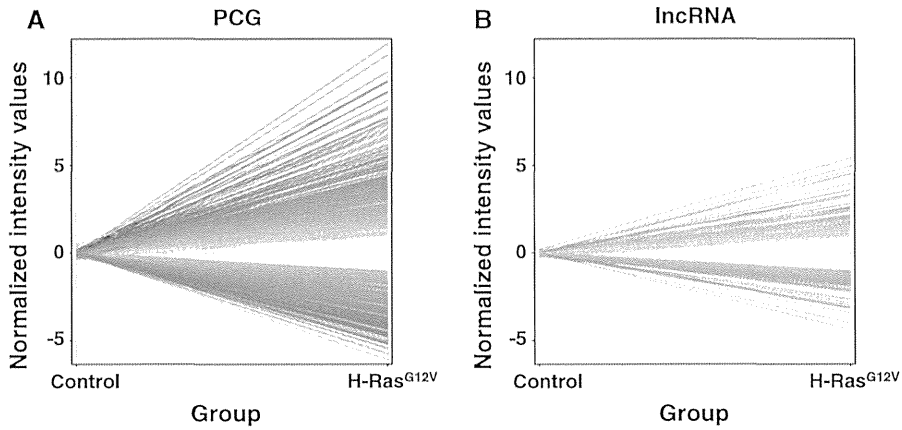

Fig. 3 Change of protein coding genes (PCG) and lncRNAs expression by oncogenic Ras. Microarray data of PCG (**a**) and lncRNAs (**b**). The mean value was calculated from triplicate samples of a representative experiment. The results are expressed relative to the corresponding values for control (WI/38Mock) cells. The vertical axis of the graph indicates fold-change against control cells (Log2). The horizontal axis of the graph indicates the sample (*left*: control cells, *right*: WI38/H-Ras^{G12V}). The graph shows data where fold-change in gene expression was greater than twofold. A p value of <0.05 was determined as significant

Table 1 Summary of microarray results for PCG and lncRNAs

	Total entity	Twofold increase entity	Twofold increase (%)	Twofold decrease entity	Twofold decrease (%)
PCG	26,608	1,513	5.7	1,860	7.0
lncRNA	7,419	243	3.3	168	2.3

(Brookes et al. 2002; Serrano et al. 1997). The reduction of *ANRIL* by oncogenic Ras might be required for the activation of *INK4* locus by oncogenic Ras, resulting in the induction of premature senescence. We also found that enforced expression of oncogenic Ras increased the expression of *PANDA*, which represses apoptosis. Mutational activation of *ras* can protect some cell strains from apoptosis (Downward 1998). The induction of *PANDA* by oncogenic Ras might be required for the repression of apoptosis, resulting in the progression of carcinogenesis. Indeed, *PANDA* is selectively increased in metastatic ductal carcinomas but not in normal breast tissue (Hung et al. 2011). It will be important issue to reveal the role of *PANDA* in carcinogenesis. However, the molecular mechanism by which oncogenic Ras regulates *ANRIL* and *PANDA* expression is unclear. Recent studies showed that E2F1 transcription factor directly binds to and activates *ANRIL* transcription (Sato et al. 2010; Wan et al. 2013). It was also revealed that several lncRNAs including *PANDA* are induced in a p53-dependent manner (Huarte et al. 2010; Hung et al. 2011). Thus, it will be important to identify the downstream effector molecules of oncogenic Ras, which regulate the expression of lncRNAs.

Although approximately 10,000 primate-specific lncRNAs have been identified (Necsulea et al. 2014), the biological functions of most lncRNAs remain unclear. This study demonstrated that the expression of many lncRNAs was altered by oncogenic Ras. Among these lncRNAs regulated by oncogenic Ras, uncharacterized functional lncRNAs associated with malignant transformation may be present.

Acknowledgments We greatly appreciate Dr. T Kitamura (The University of Tokyo, Tokyo, Japan) and Dr. CJ Der (University of North Carolina at Chapel Hill, Chapel Hill, NC, USA) for providing the plasmids used in this study. This work was supported in part by grants from the Ministry of Education, Culture, Sports, Science and Technology of Japan (to YK, KK, HN, and MK) and Takeda Science Foundation (to YK).

References

Batista PJ, Chang HY (2013) Long noncoding RNAs: cellular address codes in development and disease. Cell 152:1298–1307. doi:10.1016/j.cell.2013.02.012

Journal : Medium 10616 | Dispatch : 4-12-2014 | Pages : 5
Article No. : 9834 | ☐ LE | ☐ TYPESET
MS Code : CYTO-D-14-00229 | ☑ CP | ☑ DISK

Brookes S et al (2002) INK4a-deficient human diploid fibroblasts are resistant to RAS-induced senescence. EMBO J 21:2936–2945. doi:10.1093/emboj/cdf289

Carninci P et al (2005) The transcriptional landscape of the mammalian genome. Science 309:1559–1563. doi:10.1126/science.1112014

Downward J (1998) Ras signalling and apoptosis. Curr Opin Genet Dev 8:49–54

Fatica A, Bozzoni I (2014) Long non-coding RNAs: new players in cell differentiation and development. Nat Rev Genet 15:7–21. doi:10.1038/nrg3606

Gupta RA et al (2010) Long non-coding RNA HOTAIR reprograms chromatin state to promote cancer metastasis. Nature 464:1071–1076. doi:10.1038/nature08975

Huarte M et al (2010) A large intergenic noncoding RNA induced by p53 mediates global gene repression in the p53 response. Cell 142:409–419. doi:10.1016/j.cell.2010.06.040

Hung T et al (2011) Extensive and coordinated transcription of noncoding RNAs within cell-cycle promoters. Nat Genet 43:621–629. doi:10.1038/ng.848

Karnoub AE, Weinberg RA (2008) Ras oncogenes: split personalities. Nat Rev Mol Cell Biol 9:517–531. doi:10.1038/nrm2438

Kitagawa M, Kotake Y, Ohhata T (2012) Long non-coding RNAs involved in cancer development and cell fate determination. Curr Drug Targets 13:1616–1621

Kitagawa M, Kitagawa K, Kotake Y, Niida H, Ohhata T (2013) Cell cycle regulation by long non-coding RNAs. Cell Mol Life Sci 70:4785–4794. doi:10.1007/s00018-013-1423-0

Kotake Y, Cao R, Viatour P, Sage J, Zhang Y, Xiong Y (2007) pRB family proteins are required for H3K27 trimethylation and Polycomb repression complexes binding to and silencing p16INK4alpha tumor suppressor gene. Genes Dev 21:49–54. doi:10.1101/gad.1499407

Kotake Y, Nakagawa T, Kitagawa K, Suzuki S, Liu N, Kitagawa M, Xiong Y (2011) Long non-coding RNA ANRIL is required for the PRC2 recruitment to and silencing of p15(INK4B) tumor suppressor gene. Oncogene 30:1956–1962. doi:10.1038/onc.2010.568

Necsulea A et al (2014) The evolution of lncRNA repertoires and expression patterns in tetrapods. Nature 505:635–640. doi:10.1038/nature12943

Ruas M, Peters G (1998) The p16INK4a/CDKN2A tumor suppressor and its relatives. Biochim Biophys Acta 1378:F115–F177

Sato K, Nakagawa H, Tajima A, Yoshida K, Inoue I (2010) ANRIL is implicated in the regulation of nucleus and potential transcriptional target of E2F1. Oncol Rep 24:701–707

Schubbert S, Shannon K, Bollag G (2007) Hyperactive Ras in developmental disorders and cancer. Nat Rev Cancer 7:295–308. doi:10.1038/nrc2109

Serrano M, Lin AW, McCurrach ME, Beach D, Lowe SW (1997) Oncogenic ras provokes premature cell senescence associated with accumulation of p53 and p16INK4a. Cell 88:593–602

Sharpless NE (2005) INK4a/ARF: a multifunctional tumor suppressor locus. Mutat Res 576:22–38. doi:10.1016/j.mrfmmm.2004.08.021

Shirasawa S, Furuse M, Yokoyama N, Sasazuki T (1993) Altered growth of human colon cancer cell lines disrupted at activated Ki-ras. Science 260:85–88

Tano K et al (2010) MALAT-1 enhances cell motility of lung adenocarcinoma cells by influencing the expression of motility-related genes. FEBS Lett 584:4575–4580. doi:10.1016/j.febslet.2010.10.008

Wan G, Mathur R, Hu X, Liu Y, Zhang X, Peng G, Lu X (2013) Long non-coding RNA ANRIL (CDKN2B-AS) is induced by the ATM-E2F1 signaling pathway. Cell Signal 25:1086–1095. doi:10.1016/j.cellsig.2013.02.006

Yap KL et al (2010) Molecular interplay of the noncoding RNA ANRIL and methylated histone H3 lysine 27 by polycomb CBX7 in transcriptional silencing of INK4a. Mol Cell 38:662–674. doi:10.1016/j.molcel.2010.03.021

Journal : Medium 10616 | Dispatch : 4-12-2014 | Pages : 5
Article No. : 9834 | ☐ LE | ☐ TYPESET
MS Code : CYTO-D-14-00229 | ☑ CP | ☑ DISK

MCB
Journals.ASM.org

Fbw7 Targets GATA3 through Cyclin-Dependent Kinase 2-Dependent Proteolysis and Contributes to Regulation of T-Cell Development

Kyoko Kitagawa,[a] Kiyoshi Shibata,[b] Akinobu Matsumoto,[c] Masaki Matsumoto,[c] Tatsuya Ohhata,[a] Keiichi I. Nakayama,[c] Hiroyuki Niida,[a] Masatoshi Kitagawa[a]

Department of Molecular Biology, Hamamatsu University School of Medicine, Higashi-ku, Hamamatsu, Shizuoka, Japan[a]; Research Equipment Center, Hamamatsu University School of Medicine, Higashi-ku, Hamamatsu, Shizuoka, Japan[b]; Department of Molecular and Cellular Biology, Medical Institute of Bioregulation, Kyushu University, Higashi-ku, Fukuoka, Fukuoka, Japan[c]

Proper development of T cells depends on lineage-specific regulators controlled transcriptionally and posttranslationally to ensure precise levels at appropriate times. Conditional inactivation of F-box protein Fbw7 in mouse T-cell development resulted in reduced thymic CD4 single-positive (SP) and splenic $CD4^+$ and $CD8^+$ cell proportions. Fbw7 deficiency skewed CD8 SP lineage differentiation, which exhibited a higher incidence of apoptosis. Similar perturbations during development of CD8-positive cells were reported with transgenic mice, which enforced GATA3 (T-cell differentiation regulator) expression throughout T-cell development. We observed augmented GATA3 in CD4/CD8 double negative (DN) stage 4, CD4 SP, and CD8 SP lineages in Fbw7-deficient thymocytes. Using overexpressed proteins in cultured cells, we demonstrated that Fbw7 bound to, ubiquitylated, and destabilized GATA3. Two Cdc4 phosphodegron (CPD) candidate sequences, consensus Fbw7 recognition domains, were identified in GATA3, and phosphorylation of Thr-156 in CPD was required for Fbw7-mediated ubiquitylation and degradation. Phosphorylation of GATA3 Thr-156 was detected in mouse thymocytes, and cyclin-dependent kinase 2 (CDK2) was identified as a respondent for phosphorylation at Thr-156. These observations suggest that Fbw7-mediated GATA3 regulation with CDK2-mediated phosphorylation of CPD contributes to the precise differentiation of T-cell lineages.

The F-box protein Fbw7 (also known as Fbxw7, Sel-10, or Cdc4) forms an Skp1-cullin1-F box protein (SCF) complex that mediates the ubiquitylation of substrates. Fbw7 binds to a high-affinity recognition motif termed the Cdc4 phosphodegron (CPD), with a consensus sequence of T/S(PO_3)-P-X-X-S/T/D/E (where X indicates an arbitrary residue) (1). Fbw7 often promotes the turnover of substrates via phosphorylation of the CPD. Interestingly, many Fbw7 substrates synergize and/or function to promote specific cell differentiation. Notch1, c-Myc, and mTOR regulate quiescence and storage of hematopoietic stem cells, and Notch1, c-Myc, c-Myb, and MCL1 contribute to the development of the common lymphoid progenitor lineages (2). To investigate the role of Fbw7-mediated ubiquitylation of substrates, Fbw7 conditional knockouts were constructed with tissue-specific expression of Cre recombinase. Using gene targeting mice, some studies have reported that ablation of Fbw7 in T cells resulted in the predisposition to thymic enlargement and thymic lymphoma, which expressed both CD4 and CD8, suggesting their derivation from immature T cells, and the accumulation of c-Myc, Notch1, MCL1, and NF-κB2 (3–5). In this paper, we focused on the reduced thymic CD4 single-positive (SP) and CD8 SP and splenic $CD4^+$ and $CD8^+$ cell proportions in mice, which were conditionally depleted of Fbw7. From further detailed analysis, we found that Fbw7 deficiency also skewed the differentiation of the CD8 SP lineage, which exhibited a higher incidence of apoptosis. Interestingly, similar perturbations during development of CD8-positive cells have been reported with transgenic (Tg) mice in which expression of GATA3 was enforced throughout T-cell development (6).

T-cell progenitors undergo maturation in the thymus and subsequently migrate to the peripheral lymphoid organs. T-cell lineages of thymocytes are classified by the expression pattern of two surface antigens, CD4 and CD8. Most immature T cells do not express CD4 or CD8 and are referred to as double-negative (DN) cells. Maturation of DN cells into double-positive (DP) cells requires expression of both antigens, and further progression leads to the retained expression of CD4 or CD8 in the single-positive (SP) cells (7).

Proper development of T cells depends on lineage-specific regulators, including GATA3, which is one of the factors involved in T-cell specification and commitment. The mammalian GATA family of transcription factors comprises six types, GATA binding protein 1 (GATA1) to GATA6. While each GATA protein has a distinct and restricted tissue expression pattern, GATA1 to GATA3 are classified as the hematopoietic factors. GATA3 is expressed by immune cells. GATA3 is an important regulator of T-cell differentiation and involved in β-selection and CD4 SP T-cell development in the early stage of commitment and T helper 2 (Th2) cell maturation (8–14). GATA3 is upregulated during the development of CD4 but not CD8 SP thymocytes (15, 16). These distinctions act as one of the mediators of the CD4/CD8 lineage decision of thymocytes as overexpression of GATA3 during positive selection inhibited CD8 SP cell development (6). In addition, the increased abundance of GATA3 during the late DN stage disturbs accurate progression from DN to DP and may result in transformed cells, which are characterized as $CD4^+$ $CD8^+$ (6). GATA3 expression is regulated by Notch and NF-κB2 during Th2 differentiation (2, 17–19). We inferred that the protein degradation

Received 22 November 2013 Returned for modification 29 December 2013
Accepted 6 May 2014
Published ahead of print 12 May 2014
Address correspondence to Masatoshi Kitagawa, kitamasa@hama-med.ac.jp.

doi:10.1128/MCB.01549-13

system might play a critical role in the quantitative regulation of GATA3, similar to a transcriptional regulator. Yamashita et al. reported that extracellular signal-regulated kinase (ERK)–mitogen-activated protein kinase (MAPK) activation stabilized GATA3 through inhibition of the ubiquitin (Ub)-proteasome signaling and that Mdm2 was involved in the ubiquitylation of GATA3 in T cells although the involvement for phosphorylation in regulation by Mdm2 has not been elucidated (20).

We found that GATA3 protein accumulated in T-cell lineages of Fbw7-deficient thymocytes. With the identification of two candidate CPD sequences in GATA3 and given that Fbw7 plays crucial roles in the development of T-cell lineages through the regulation of transcription factors, we hypothesized that Fbw7 targets GATA3 and that its interaction, which is regulated by cyclin-dependent kinase 2 (CDK2)-mediated phosphorylation of CPD, modulates the development of T-cell lineages.

MATERIALS AND METHODS

Conditional knockout mice. The generation and genotyping of conditional knockout Lck-Cre/*Fbw7*$^{flox/flox}$ mice were described previously (3). Mice 6 to 10 weeks of age were used for analysis. All mice were treated according to the protocols approved by the Hamamatsu University School of Medicine Animal Care Committees at the Center Animal Care facility.

Cell culture. Whole thymocytes obtained from *Fbw7*$^{flox/flox}$ or Lck-Cre/*Fbw7*$^{flox/flox}$ mice and HUT78 cells (Riken) were cultured in RPMI 1640 medium supplemented with 10% fetal bovine serum, penicillin (100 U/ml), and streptomycin (100 μg/ml). HEK293 and HeLa cells were maintained in Dulbecco's modified Eagle's medium (DMEM) supplemented with 10% fetal bovine serum, penicillin (100 U/ml), and streptomycin (100 μg/ml).

Generation of P-T156-GATA3 antibody. Polyclonal antibodies against phosphorylated Thr-156 of GATA3 (P-T156-GATA3) were raised against a keyhole limpet hemocyanin (KLH)-conjugated chemically synthesized phosphorylated Thr-156 peptide (P-T156 peptide), corresponding to the CPD region of GATA3 (residues 150 to 161) (MBL). Antiserum obtained from an immunized guinea pig was purified using column chromatography conjugated with the P-T156 peptide and then passed through a column conjugated with nonphosphorylated Thr-156 peptide (Peptide Institute) to eliminate antibodies against nonphosphorylated Thr-156 peptide. The antibody specificity was confirmed by enzyme-linked immunosorbent assay and immunoblotting.

Antibodies and fluorescence-activated cell sorting (FACS) analysis. Phycoerythrin (PE)-Cy5-conjugated anti-CD4 (RM4-5), fluorescein isothiocyanate (FITC)-conjugated anti-CD8a (53-6.7), and PE-labeled annexin V were purchased from BD Pharmingen. PE-Cy7-conjugated anti-CD44 (IM7) and Alexa Fluor 700-conjugated anti-CD25 (PC61) were also purchased from Biolegend. After cell surface labeling, thymic T cells and splenic T cells of mice were scored and sorted by FACS Aria instruments (BD). In addition, anti-Myc 9B11 (Cell Signaling), anti-Myc 9E10 (Roche), anti-FLAG M2 (Sigma), antihemagglutinin (anti-HA) 3F10 (MBL), anti-GATA3 HG3-31 (Santa Cruz), anti-Fbw7 (catalog number A301-720A; Bethyl), anti-CDK2 (TDL), antiphosphothreonine (catalog number 71-8200; Invitrogen), anti-glutathione S-transferase (anti-GST) (B-14; Santa Cruz), anti-HSP90 (catalog number 610419; BD), anti-α-tubulin (clone DM1A; Sigma), anti-β-actin (clone AC15; Sigma), and anti-NF-κB2 (catalog number A301-822A; Bethyl) were also purchased for immunoblot analysis. Alexa Fluor 546-conjugated anti-GATA3 was prepared by an Alexa Fluor 546 monoclonal antibody labeling kit (Zenon).

ICC analysis. Immunocytochemistry (ICC) was performed on cytospin preparations of the sorted cell subpopulations. Cells were incubated overnight with Alexa Fluor 546-conjugated anti-GATA3 antibody at 4°C, followed by 4′,6′-diamidino-2-phenylindole (DAPI) staining. The relative protein levels were calculated as the means ± standard deviations (SD) from 10 random areas.

Plasmids, recombinant proteins, and protein kinases. Complementary DNAs encoding wild-type (WT) and mutant GATA3 were cloned into pcDNA3.1/Myc-His (Invitrogen). FLAG-tagged Fbw7 was cloned into pcDNA3.1 (Invitrogen). The expression plasmid for ubiquitin (pCGN-HA-Ub) was previously described (21). All point mutants of GATA3 were constructed using standard recombinant DNA techniques. Glutathione *S*-transferase (GST) and GST-fused GATA3 proteins were expressed in *Escherichia coli* BL21 and affinity purified with glutathione-Sepharose 4B (GE Healthcare). The fusion proteins were eluted with 10 mM reduced glutathione. Recombinant protein kinases used in the *in vitro* phosphorylation assay were cyclin E/CDK2 (Abcam), cyclin D1/CDK4 (Abcam), cyclin D2/CDK4 (Abcam), cyclin A/CDK2 (Abcam), cyclin B/CDK1 (Abcam), ERK1 (Carna Biosciences), p38α (Carna Biosciences), HIPK2 (Carna Biosciences), NLK (Carna Biosciences), and glycogen synthase kinase 3β (GSK3β; NEB). For the *in vitro* binding assay, recombinant cyclin A/CDK2 (Carna Biosciences) and p38α (Millipore) were used.

Immunoprecipitation and ubiquitylation assay. Plasmids were transiently transfected into HEK293 cells by the calcium phosphate method. After 43 h, cells were treated with 20 μM MG132 (Peptide Institute) for 5 h and subsequently lysed in lysis buffer containing protease inhibitors. For immunoprecipitation (IP), cell lysates were incubated with antibodies and protein G-Sepharose 4FF (GE Healthcare) at 4°C. Immunocomplexes were washed with lysis buffer. For denaturing and IP analysis, lysates from plasmid-transfected HEK293 or HeLa cells were denatured by the addition of SDS sample buffer and incubation at 100°C for 8 min before being incubated with an anti-Myc antibody and protein G-Sepharose 4FF at 4°C. Immunoprecipitated samples as well as the original cell lysates (input) were separated by SDS-PAGE and transferred from the gel onto a polyvinylidene difluoride (PVDF) membrane (Millipore), followed by immunoblotting. Proteins were visualized using an enhanced chemiluminescence system (PerkinElmer).

Degradation assay. Plasmids were transfected into HeLa cells. At 24 h after transfection, each transfection was replated into five culture dishes for the chase experiment, and after an additional 24 h, cells were treated with 12.5 mg/ml of cycloheximide for the times indicated in Fig. 6. Cell lysates were subjected to immunoblotting. The intensity of the bands was quantitated using the image analysis software Image Gauge, version 4.21 (Fujifilm), and the signal intensity of each GATA3 protein was normalized using levels of HSP90 as a loading control.

***In vitro* phosphorylation assay.** GATA3 WT peptide or GATA3-T156A peptide (0.1875 mM) was incubated with 0.1 μg of recombinant kinase at 30°C for 1 h in reaction buffer containing 50 μM ATP and 3.5 μCi of [γ-^{32}P]ATP (6,000 Ci/mmol), in a final volume of 20 μl. Reactions were terminated by the addition of 10 μl of 250 mM H_3PO_4. Peptides were trapped on P81 papers (Whatman), which were washed six times with 75 mM H_3PO_4 and then monitored for radioactivity in a liquid scintillation counter, as previously described (22). A purified GST-fused WT or T156A mutant of GATA3 was incubated with the kinase sources indicated in Fig. 7 and 8 at 30°C for 30 min in reaction buffer containing 63 mM ATP. CDK2 inhibitor (CVT313; Enzo Life Sciences) or competitor (purified recombinant p27) at the indicated dose was added before incubation. The reaction was terminated by boiling mixtures for 5 min. For *in vitro* phosphorylation and binding assays, instead of boiling, phosphorylated mixtures were incubated for an additional hour at 4°C with lysate from HEK293 cells exogenously expressing Fbw7. GST-fused proteins were then precipitated using glutathione-Sepharose beads. All reaction mixtures were subjected to immunoblot analysis using the indicated antibody.

RNA interference. HEK293 cells were transfected with GATA3 expression plasmid and small interfering (siRNA) oligonucleotides for CDK2 using Lipofectamine 2000 reagent (Life Technologies), according to the manufacturer's protocol. After 43 h, cells were treated with 20 nM

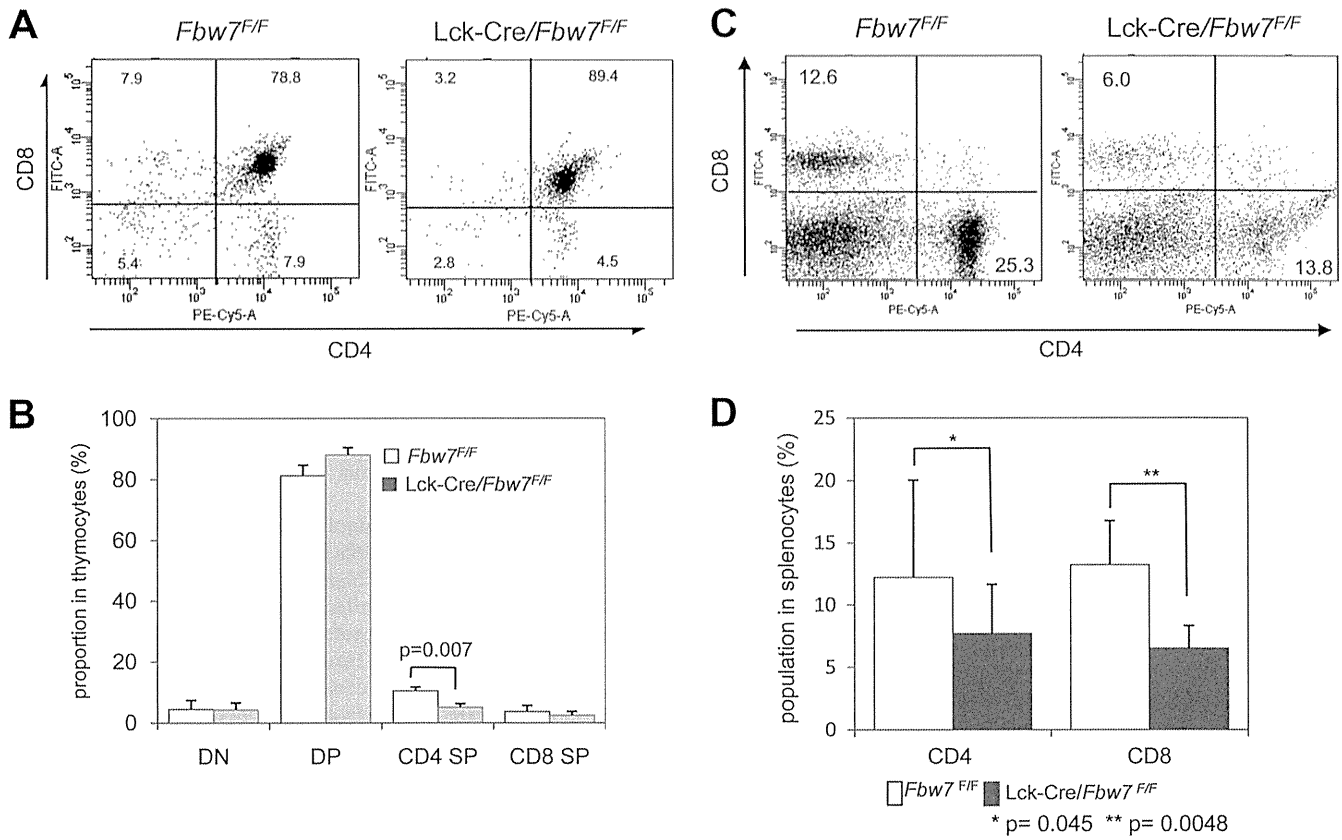

FIG 1 The CD4 SP subset in the thymus and CD4$^+$ and CD8$^+$ T-cell subpopulations in the spleen of Lck-Cre/*Fbw7*$^{flox/flox}$ mice are reduced. (A) Representative flow cytometric analysis of surface expression of CD4 and CD8 on thymocytes from *Fbw7*$^{flox/flox}$ or Lck-Cre/*Fbw7*$^{flox/flox}$ mice at 8 weeks of age. The percentages of DN, DP, and SP populations are indicated. (B) Proportions of the T-cell subsets determined in panel A. Data are means ± SD from six mice of each genotype. (C) Representative flow cytometric analysis of surface expression of CD4 or CD8 on splenocytes from *Fbw7*$^{flox/flox}$ or Lck-Cre/*Fbw7*$^{flox/flox}$ mice at 9 to 10 weeks of age. The percentages of CD4$^+$ and CD8$^+$ T-cell subpopulations are indicated. (D) Proportions of the T-cell subsets determined in panel C. Data are means ± SD from six mice of each genotype. The *P* value was determined using the Student *t* test. F/F, flox/flox.

okadaic acid and 20 μM MG132 for 5 h. The nucleotide sequence of the CDK2 siRNA was 5′-AAGGUGGUGGCGCUUAAGAAA-3′ with 3′ dTdT overhangs (Sigma Genosys). Cell lysates were subjected to immunoblotting.

qRT-PCR analysis. Total RNA was isolated from cells using RNAiso (TaKaRa) or Isogen-LS (Wako) and subjected to reverse transcription with random hexanucleotide primers and SuperScript II reverse transcriptase (Invitrogen). The resulting cDNA was subjected to quantitative real-time PCR (qRT-PCR) using a Rotor-Gene 3000 system (Corbett Research) and a SYBR premix *Ex Taq* kit (TaKaRa). The sequences of PCR primers were as follows: 5′-AGGCAGGGAGTGTGTGAACT-3′ (sense) and 5′-TCATAGTCAGGGGTCTGTTA-3′ (antisense) for GATA3; 5′-CAGGGAAACCCAGGAAAAAC-3′ (sense) and 5′-AGTTCCGCACATCCTTCTTG-3′ (antisense) for CCR7; 5′-AGAAGAGGGGATTGATGAAC-3′ (sense) and 5′-AGTGTTGTCATCAGAACCAC-3′ (antisense) for Fbw7; 5′-TGCACCACCAACTGCTTAG-3′ (sense) and 5′-CAGGCAGGGATGATGTTC-3′ (antisense) for glyceraldehyde-3-phosphate dehydrogenase (GAPDH). The amount of transcript was normalized against that of GAPDH as an internal standard.

Cell cycle synchronization. For arrest during G_1/S phase, HeLa cells were incubated with 1 μg/ml aphidicolin (Sigma) for 16 h, incubated in aphidicolin-free medium for 10 h, and then incubated with 1 μg/ml aphidicolin for 16 h. For arrest in G_2/M phase, HeLa and HUT78 cells were incubated with 1 μg/ml aphidicolin for 16 h, incubated in aphidicolin-free medium for 4 h, and then incubated with 100 ng/ml nocodazole (Sigma) for 16 h. The DNA content of HUT78 cells nonsynchronized or synchronized at G_2/M phase was examined by flow cytometry after propidium iodide staining (Beckman Coulter).

RESULTS

Conditional inactivation of Fbw7 in the T-cell lineages impedes T-cell development. To address the unknown *in vivo* contribution of Fbw7 to T-cell development, we used conditional knockout Lck-Cre/*Fbw7*$^{flox/flox}$ mice, which lost Fbw7 expression from genetic deletion by Cre recombinase activity under the control of the Lck promoter (3). We found a significant decrease in the CD4 SP cell proportion in Lck-Cre/*Fbw7*$^{flox/flox}$ mice compared with *Fbw7*$^{flox/flox}$ mice (Fig. 1A and B). Moreover, we observed a tendency toward a reduction of the CD8 SP and an increase of the DP cells as a proportion of the thymocyte population (Fig. 1A and B). To determine the influence of the ablation of Fbw7 on the development of peripheral T cells, we examined spleens harboring CD4$^+$ and CD8$^+$ T cells from *Fbw7*$^{flox/flox}$ and Lck-Cre/*Fbw7*$^{flox/flox}$ mice. The percentages of both CD4$^+$ and CD8$^+$ cells were significantly reduced in the spleen of Lck-Cre/*Fbw7*$^{flox/flox}$ mice compared with *Fbw7*$^{flox/flox}$ control mice (Fig. 1C and D). Because the CD4 SP subtype in the thymus of Lck-Cre/*Fbw7*$^{flox/flox}$ mice was significantly reduced, it might affect the splenic CD4$^+$ T cells. Our results suggest that the aberrant accumulation of an Fbw7 substrate, which may be GATA3, in CD8 SP cells from Lck-Cre/Fbw7$^{flox/flox}$ mice might be

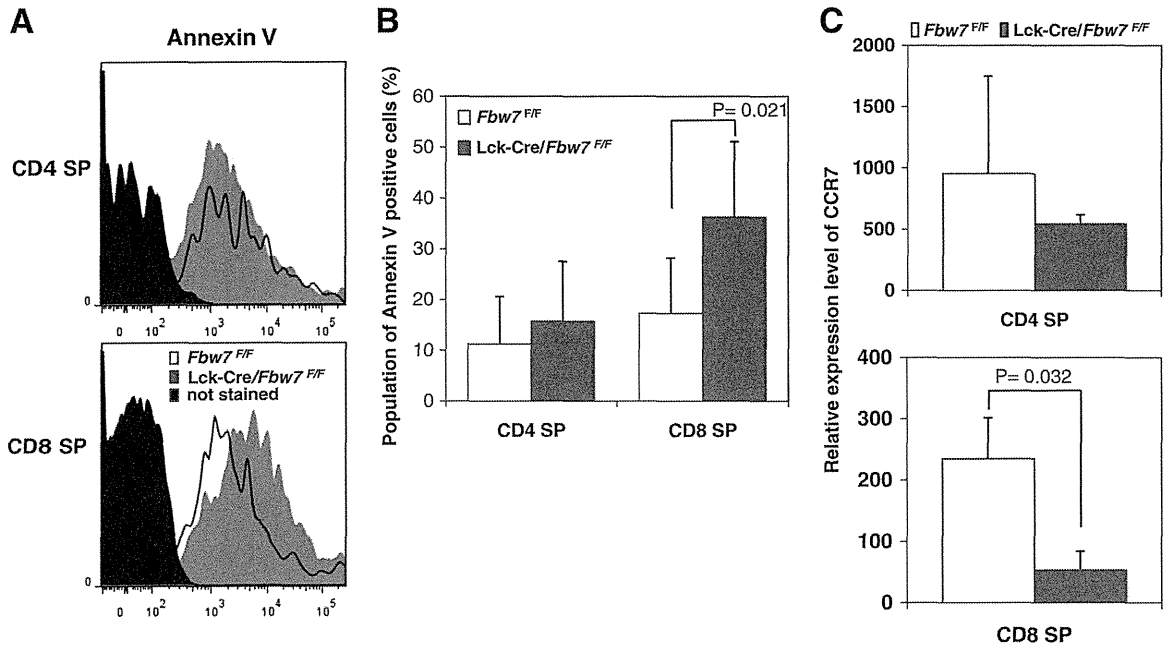

FIG 2 Defects in T-cell maturation in Lck-Cre/*Fbw7*$^{flox/flox}$ mice. Apoptotic levels in SP subpopulations from *Fbw7*$^{flox/flox}$ and Lck-Cre/*Fbw7*$^{flox/flox}$ mice were evaluated. (A) Graphs show representative profiles of annexin V staining in CD4 SP and CD8 SP subsets from both groups of mice at 8 to 9 weeks. (B) Percentage of annexin V-positive cells determined from panel A. Data are means ± SD from the percentage of annexin V staining in CD4 SP and CD8 SP subsets from five *Fbw7*$^{flox/flox}$ and six Lck-Cre/*Fbw7*$^{flox/flox}$ mice. The *P* value was determined using the Student *t* test. (C) The relative expression level of CCR7 in CD4 SP and CD8 SP subsets in the thymus from *Fbw7*$^{flox/flox}$ or Lck-Cre/*Fbw7*$^{flox/flox}$ mice at 8 to 9 weeks of age. CCR7 levels were measured by qRT-PCR and normalized against GAPDH as an internal standard. Data are means ± SD from three mice of each genotype.

due to enhanced apoptosis and/or perturbed maturation at the final differentiation stage in the thymus.

We next examined the fraction of annexin V-positive cells in the SP subpopulation in thymocytes of Lck-Cre/*Fbw7*$^{flox/flox}$ and *Fbw7*$^{flox/flox}$ mice. Although no clear differences in annexin V-positive CD4 SP cell populations was observed, we found significantly more annexin V-positive CD8 SP cells in Lck-Cre/*Fbw7*$^{flox/flox}$ mice than in control mice (Fig. 2A and B). Previously, mice with enforced GATA3 expression throughout T-cell development, driven by the CD2 locus control region (CD2-GATA3 Tg mice), contained higher numbers of apoptotic cells in the thymus, especially in CD8 SP cells, than in the controls and decreased CD8$^+$ T-cell numbers in the periphery although total numbers of CD8 SP cells in the thymus were within normal ranges compared with controls (6). Our findings of aberrations in Lck-Cre/*Fbw7*$^{flox/flox}$ mice corresponded well with those observed in CD2-GATA3 Tg mice. These data imply that excess GATA3 in the CD8 SP subpopulation in the thymus may cause the distinctive aberrations observed in CD8$^+$ splenocytes.

Newly generated SP thymocytes migrate from the thymic cortex to the medulla, where they undergo functional maturation to acquire immune competence and egress capability (23, 24). CC-chemokine receptor 7 (CCR7) is an important receptor for the medullary positioning of SP cells and an indispensable signal mediator for unperturbed thymic T-cell differentiation and maturation (24, 25). CCR7 remains at low levels in newly generated SP cells and is quickly upregulated and maintained at high levels afterwards (26). CD8$^+$ CCR7$^-$ T cells are more sensitive to spontaneous apoptosis than CD8$^+$ CCR7$^+$ T cells (27). This suggests that insufficient CCR7 in CD8$^+$ SP cells suppresses final maturation in the thymus, followed by an induction of apoptosis (27). We speculated that reduced CCR7 expression could be involved in defects in development and survival of CD8 SP cells in the thymus of Lck-Cre/*Fbw7*$^{flox/flox}$ mice and next evaluated CCR7 expression in SP cells of Lck-Cre/*Fbw7*$^{flox/flox}$ and *Fbw7*$^{flox/flox}$ mice. Significant reduction of CCR7 expression was detected in CD8 SP cells from Lck-Cre/*Fbw7*$^{flox/flox}$ mice compared with expression in *Fbw7*$^{flox/flox}$ mice although loss of Fbw7 did not affect the relative expression level of CCR7 in CD4 SP cells (Fig. 2C). Normal CD8 SP cells harbor lower GATA3 levels and may be associated with reduced CCR7 transcription. Finally, we speculate that repression of CCR7 caused by the accumulation of GATA3 in CD8 SP cells resulted in the prevention of final maturation and survival in the thymus of the Lck-Cre/*Fbw7*$^{flox/flox}$ mice.

Loss of Fbw7 causes accumulation of GATA3 during T-cell differentiation in the thymus. GATA3 gene expression is required during T-cell differentiation from early to late stages in the thymus (28). To examine the *in vivo* contribution of Fbw7 to GATA3 stability during T-cell development, we examined the expression level of GATA3 in subsets of thymocytes. CD4 SP and especially DN and CD8 SP subsets from Lck-Cre/*Fbw7*$^{flox/flox}$ mice displayed marked increases in GATA3 protein levels compared with cells from *Fbw7*$^{flox/flox}$ mice, whereas an increase of GATA3 in comparison with the level in control animals was not observed in the DP lineage of Fbw7-deficient mice (Fig. 3A).

Fbw7 protein was detected throughout the stages of T-cell differentiation in control mice and was abolished in DP, CD4 SP, and CD8 SP subsets of Lck-Cre/*Fbw7*$^{flox/flox}$ mice although it was detectable in DN subsets (Fig. 3A). A previous report showed that Lck-Cre-mediated inactivation of the floxed allele